AD-A057 791 FRANKLIN INST RESEARCH LABS PHILADELPHIA PA F/G 13/9
DEVELOPMENT OF COMPLIANT-MOUNTED GAS-LUBRICATED JOURNAL BEARING--ETC(U)
JUL 78 W SHAPIRO, R COLSHER N00014-78-C-0119
UNCLASSIFIED FIRL-I-C4965 NL

1 OF 1
AD
A057791

END
DATE
FILMED
10-78
DDC

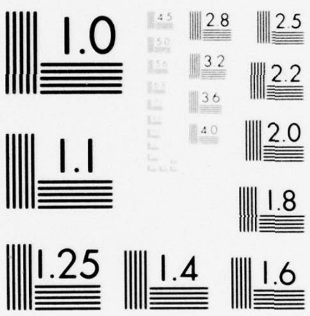

MICROCOPY RESOLUTION TEST CHART
NATIONAL BUREAU OF STANDARDS-1963-A

12

Technical

Report

I-C4965

July 1978

DEVELOPMENT OF COMPLIANT-MOUNTED GAS-LUBRICATED JOURNAL BEARINGS WITH HIGH-SPEED, HIGH-LOAD CAPABILITY

By

W. Shapiro
R. Colsher

Contract N00014-78-C-0119

THE FRANKLIN INSTITUTE RESEARCH LABORATORIES
THE BENJAMIN FRANKLIN PARKWAY · PHILADELPHIA, PENNSYLVANIA 19103

Contract N00014-78-C-0119 new
⑮

Technical

⑭ FIRL-I-C4965

Report

⑨ Technical rept.,

⑥

DEVELOPMENT OF COMPLIANT-MOUNTED GAS-LUBRICATED JOURNAL BEARINGS WITH HIGH-SPEED, HIGH-LOAD CAPABILITY.

By

⑩ W./Shapiro
R./Colsher

⑪ Jul 78

⑫ 64p.

THE FRANKLIN INSTITUTE RESEARCH LABORATORIES.
THE BENJAMIN FRANKLIN PARKWAY · PHILADELPHIA, PENNSYLVANIA 19103

78 07 03 030
142 925 LB

ABSTRACT

The report describes the development of compliant-mounted or, more accurately, compliant-pivot journal bearings. Bearings of 1.4 inches and 1.8 inches in diameter (L/D = 1) operated without whirl at 76,000 rpm. An inadvertent test malfunction subjected the bearings to shock loading which they sustained without significant damage. The 1.4 inch diameter bearing was loaded to approximately 19 psi at 60,000 rpm when journal contact occurred. Overloading produced obvious bearing wipe, but the bearing was re-run without re-work and performed satisfactorily.

CONTENTS

FIGURES

FIGURES (Continued)

TABLES

NOMENCLATURE

A = Area of elastomer pad, in^2

C = Machined clearance of pad, in.

C_L = Non-dimensional pad load coefficient = P/P_aRL

D = Journal diameter, in.

E = Modulus of elasticity of elastomer, lbs/in

e' = Shaft displacement from dead-end position, in.

f_b = Bending load factor

f_c = Compression load factor

g_1, g_2 = Elastomer stiffness factors

H_p = Non-dimensional pivot film thickness = h_p/C

h_p = Pivot film thickness, in.

I_p = Pitch inertia of pad, $lb\text{-}in\text{-}sec^2$

$\bar{I}_p$ = Non-dimensional pad pitch inertia = $I_pC\Omega^2/(4P_aR^3L)$

K = Radius of gyration of elastomer area about bending axis, in.

K_R = Elastomer radial stiffness, lbs/in

K_S = Beam or cantilever spring stiffness of top pad, lbs/in

K_T = Pad support torsional stiffness

L = Bearing length, in.

ℓ = Thickness of elastomer

M_f = Non-dimensional pad friction coefficient = M_f/P_aRLC

m_f = Pad viscous friction moment, in-lbs

NOMENCLATURE (Continued)

M_s = Non-dimensional journal mass = $I_p C\Omega^2/(4P_a R^3 L)$

m_s = Journal mass, lb-sec^2/in

P_a = Ambient pressure, psia

P_B = Fluid-film load of bottom pad, lbs

P_o = Dead weight position preload of top pad, lbs

P_T = Fluid-film load of top pad, lbs

R = Journal radius, in.

S = Elastomer durometer

W = Bearing load, lbs

W_g = Gravity load of shaft, lbs

α = Angular extent of pad, deg.

β = Angle from load vector to pivot position

Λ = Non-dimensional compressibility parameter = $6\mu\Omega(R/C)^2/P_a$

μ = Fluid viscosity, lb-sec/in^2

ϕ = Angle from leading edge of pad to pivot, deg.

Ω = Journal speed, rad/sec

1. INTRODUCTION

One of the most prominent types of gas-lubricated journal bearings has been the pivoted pad bearing. It has the necessary quality of being whirl-resistant and it is one of the few types of bearings that can operate in a high speed gaseous environment without whirling. It has the disadvantages of mechanical pivots which are subject to fretting corrosion, load limitations especially at start-up, and expensive material combination coatings for high-speed rub capability.

To circumvent these difficulties, FIRL has been developing [1], [2], [3]* the compliant-mounted or compliant-pivot bearing.

The configuration is shown on Figure 1-1. A bearing assembly consists of a bearing retainer and three 100° arc pads. The pads are made of carbon-graphite bonded to a steel outer shell. The pad material is a dense carbon with a lubricating binder. It is manufactured by Pure Carbon Corp. of St. Mary's, Pennsylvania; the carbon material designation is P6452. This material demonstrated excellent start-stop and high-speed rub characteristics in various laboratory tests at FIRL. The top shoe is mounted to a beam spring to allow centrifugal and thermal expansions to be accommodated in a predictable and well-controlled manner. The spring also alleviates manufacture of close tolerance installation clearances as some pre-load is allowed at zero speed conditions.

Note that between the elastomer and the pad a corrugated heat exchanger is incorporated. Air flowing through this exchanger removes the heat of viscous friction and precludes it from overheating the elastomer.

---

*Bracketed numbers apply to references in Section 7.

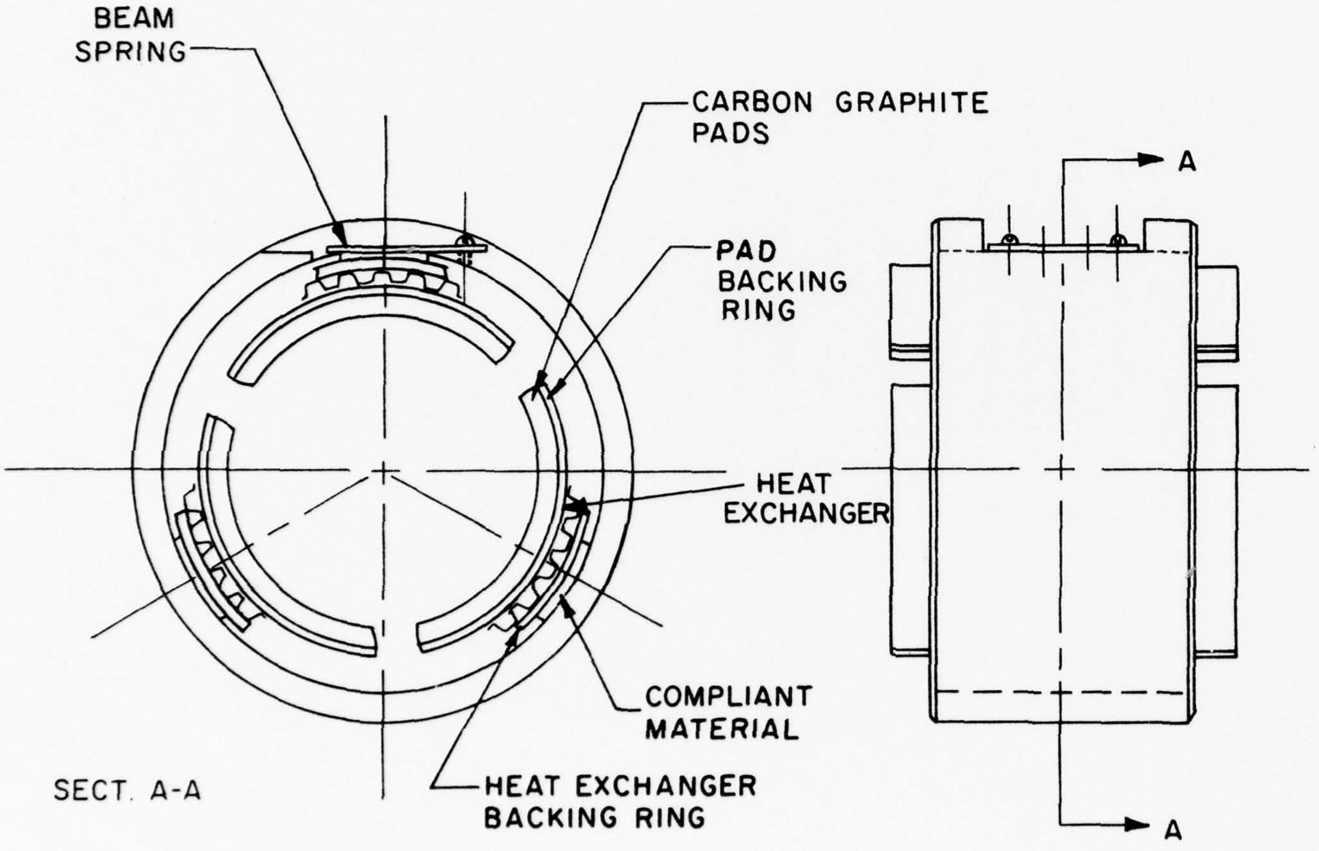

Figure 1-1. Spring-Mounted Compliant-Pivot Journal Bearing

The advantages of the compliant-pivot configuration are:

- Load Capacity - Because the pads are rigid, the clearance, preload, and pivot position can be optimized for load capacity, and the load capability of these bearings can match or exceed their rigid counterparts.

- Start-Stop Characteristics - Since the pads can move radially as well as pitch, fluid-film formation occurs very rapidly which minimizes wear at start-up and shutdown.

- Alignment - The pads can move in the roll direction (normal to direction of sliding) so that the bearings can readily align to a tilted shaft or thrust collar.

- Tolerance to Contamination - If contaminant enters the clearance region, the surface can give radially and this permits the contaminant to be carried through to the grooves between pads where it is flushed out of the bearing.

- Stability - Compliant mounted bearings have all the inherent stability characteristics of tilting-pad bearings.

- Damping - The elastomer substrate provides damping in the pad support which helps to suppress rotor vibrations. Also, substrate damping prevents excessive pad vibrations in the pitch mode.

- Pivots - The elastomer pivots avoid the complexities of expensive ball and socket configurations and the pivot fretting corrosion problems which occur in high-speed applications.

- Material Combinations - With compliant-mounted bearings, it is possible to use pad materials that have good rubbing qualities. Conventional bearings are often confined to using materials similar to the shaft journal so that the bearing and journal expand together. For the compliant mounted bearing, this restraint can be eliminated provided the stiffness of the fluid film exceeds that of the elastomer substrate.

- Space - In general, the compliant-mounted bearing will not consume as much space as contemporary ball and socket pivot bearings.

The disadvantages of the compliant-pivot configuration are:

- Temperature - Temperature limitations of elastomers are the most restricting factor with respect to the use of compliant-mounted bearings. For most elastomers, a temperature limit of 300 to 350 F is acceptable; with Silicones, it is possible to go as high as 450 F.

- Thermal Expansions - It is important to recognize that the coefficient of thermal expansion of an elastomer is approximately 10 times that of steel. Thus, from pure considerations of thermal expansion, the tendency would be for the pads to clamp against the shaft. However, as long as the film stiffness exceeds that of the elastomer, or other pad mounting, this danger is avoided, and the pitch, roll, and radial motion capabilities of the elastomer are very beneficial in permitting the bearing to accommodate thermal expansions and distortions.
- Stiffness - The elastomer mount and beam spring reduce the radial stiffness of the bearing as compared to rigid mounts.

Both high-speed and load testing were accomplished on bearings of 1.4 inch and 1.8 inch diameter (L/D = 1). Since the 1.4 inch diameter bearing was subjected to the heavier psi loading, it is the bearing that receives the major share of attention in this report. Following are a description of the design features and dimensions, theoretical performance and a discussion of the test program and results.

2. BEARING DESIGN FEATURES AND DIMENSIONS

Two bearings of differing sizes were manufactured and tested. Design drawings for both bearings are shown on Figures 2-1 and 2-2. The effective bearing dimensions are L/D = 1, with the finished pad diameter of the smaller bearings equal to 1.4 inches and that of the larger bearing equal to 1.8 inches. A tabulation of specific design parameters are shown on Table I.

To improve stability the following rationale went into the final design:

- The pitch inertia of the pads was minimized. The bearing pads were made as light as possible, especially at the leading and trailing edges.

- The pitch stiffness of the rubber was reduced as much as possible to allow the pads to pitch freely. A design goal for the pitch stiffness of the rubber was 1/5 to 1/10 of the film pitch stiffness. The angular extent of the elastomer was kept to a minimum and the elastomer thickness was selected so that the proper radial stiffness was obtained.

To prevent incompatible thermal expansions the design included the following:

- One of the three bearing pads incorporated a mechanical spring with a "soft" spring constant. The spring stiffness was selected so that large thermal growth could occur without loading the bearing severely.

- Since rubber expands approximately 10 times more than steel, the rubber thickness was kept to a minimum.

- A heat shield was incorporated between the pad and the rubber, to allow the maximum surface area for the heat to escape.

- The cold manufactured, machined in clearance (difference in curvature of the pads and curvature of the shaft) was selected so that at design speeds and temperatures the resulting hot clearances were optimum.

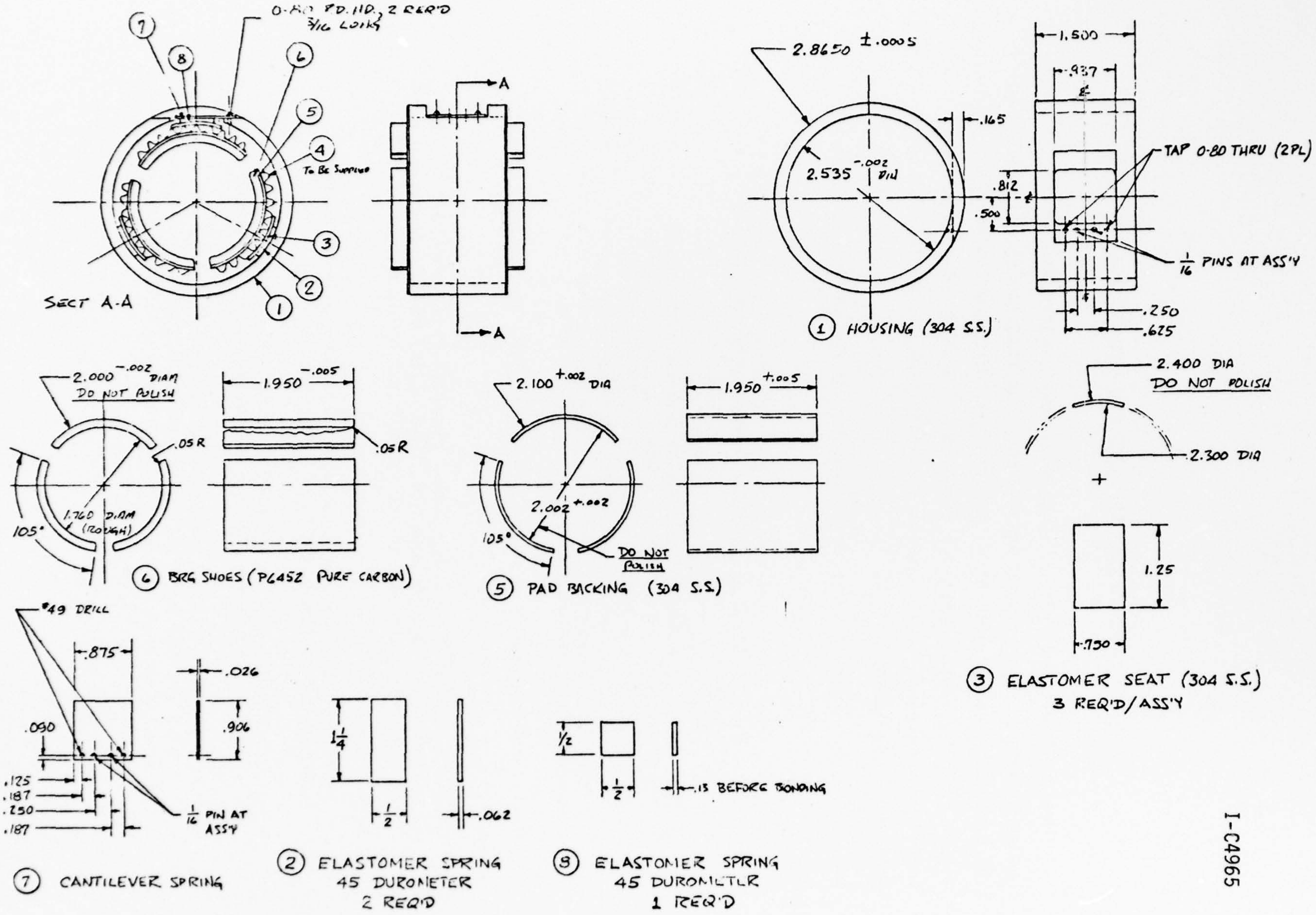

I-C4965

Figure 2-1. Small Journal Bearing, Design Drawing, Dia. = 1.4 inches

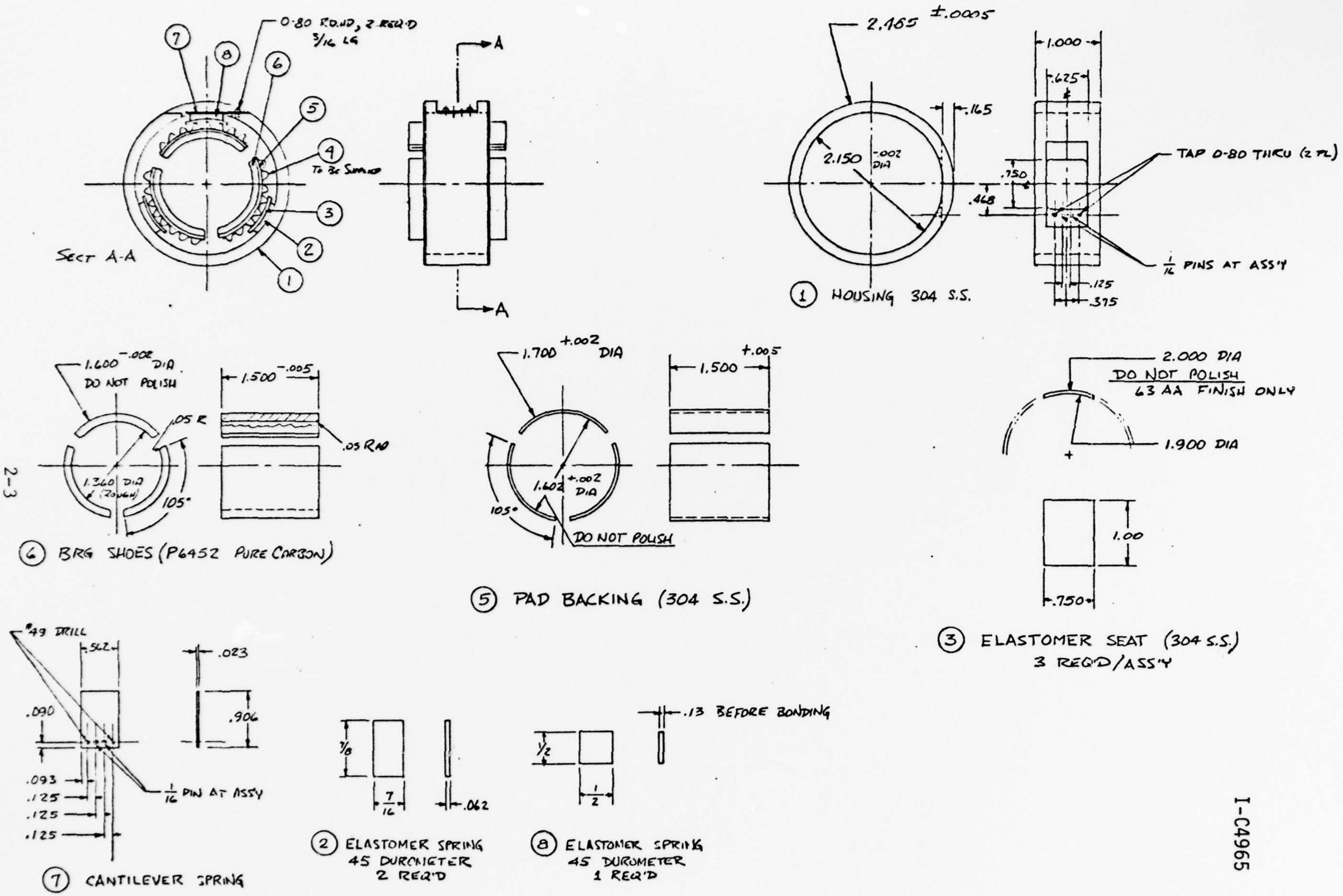

Figure 2-2. Large Journal Bearing, Design Drawing, L/D = 1, Dia. = 1.8 in.

Table I. Final Design Parameters of Spring-Mounted, Compliant Pivot Journal Bearings

	Inboard End	Outboard End
Length	1.8 in.	1.4 in.
Diameter	1.8 in.	1.4 in.
$C\ (\text{cold})_{rad}$	.0035-.004"	.00275-.00325"
$C\ (\text{hot})_{rad}$	.0025	.002
Set-up Preload	0-2 lbs	0-2 lbs
Mech. Spring Stiffness	600 lb/in	500 lb/in
Elastomer Material	Silicone Rubber (45 durometer)	
Rubber Shape	Rectangular (1 piece)	
Rubber Thickness	1/16"	1/16"
Rubber Pitch Stiffness	300-500 in-lb/rad	150-250 in-lb/rad
Rubber Radial Stiffness	20,000-30,000 lb/in	8000-12,000 lb/in
Pad Material	Pure Carbon P6452 graphite	
Pad Pitch Inertia	$.92 \times 10^{-4}$ lb-in-sec^2	$.44 \times 10^{-4}$ lb-in-sec^2
Carbon Thickness	.12 in.	.12 in.
Steel Backing for Carbon	.05 in.	.05 in.
Steel Backing for Corrugation	.05 in.	.05 in.
Corrugation Thickness	.1 in.	.1 in.

3. THEORETICAL PERFORMANCE OF THE 1.4-INCH SQUARE BEARING

3.1 MATHEMATICAL MODEL

Figure 3-1 shows the mathematical model used for generating steady state performance of the compliant-pivot bearing. It consists of three pivoted pads, each supported by radial and torsional springs at the pivot position. The spring stiffnesses of the two bottom pads correspond to the elastomer stiffness, while that of the top pad corresponds to the beam spring stiffness.

For steady-state performance a solution is satisfied, for any operating position of the shaft, when the radial forces and torques about the pivot of each pad are in equilibrium.

3.2 FLUID-FILM PERFORMANCE

Since the compliant pivots have been designed to provide practically frictionless restraint, accurate performance can be obtained by utilizing fluid-film performance information that neglects moment restraint about the pivot position. Equilibrium for each individual pad is satisfied by equating the radial force of the fluid-film through the pivot position to that of the support spring.

Non-dimensional fluid-film performance curves generated from computer codes are shown on Figures 3-2 and 3-3. They show non-dimensional pad load coefficient and friction moment as a function of pivot film thickness and the compressibility parameter Λ. As can be seen from the curves, for high-load conditions or for small values of the pivot-film thickness it is difficult to extrapolate data from these curves since they tend to become asymptotic to the ordinate axis. Therefore, curves of the reciprocal of the pad-load coefficient C_L and pad friction moment coefficient M_f were generated. It is easier to extrapolate the inverse parameters

I-C4965

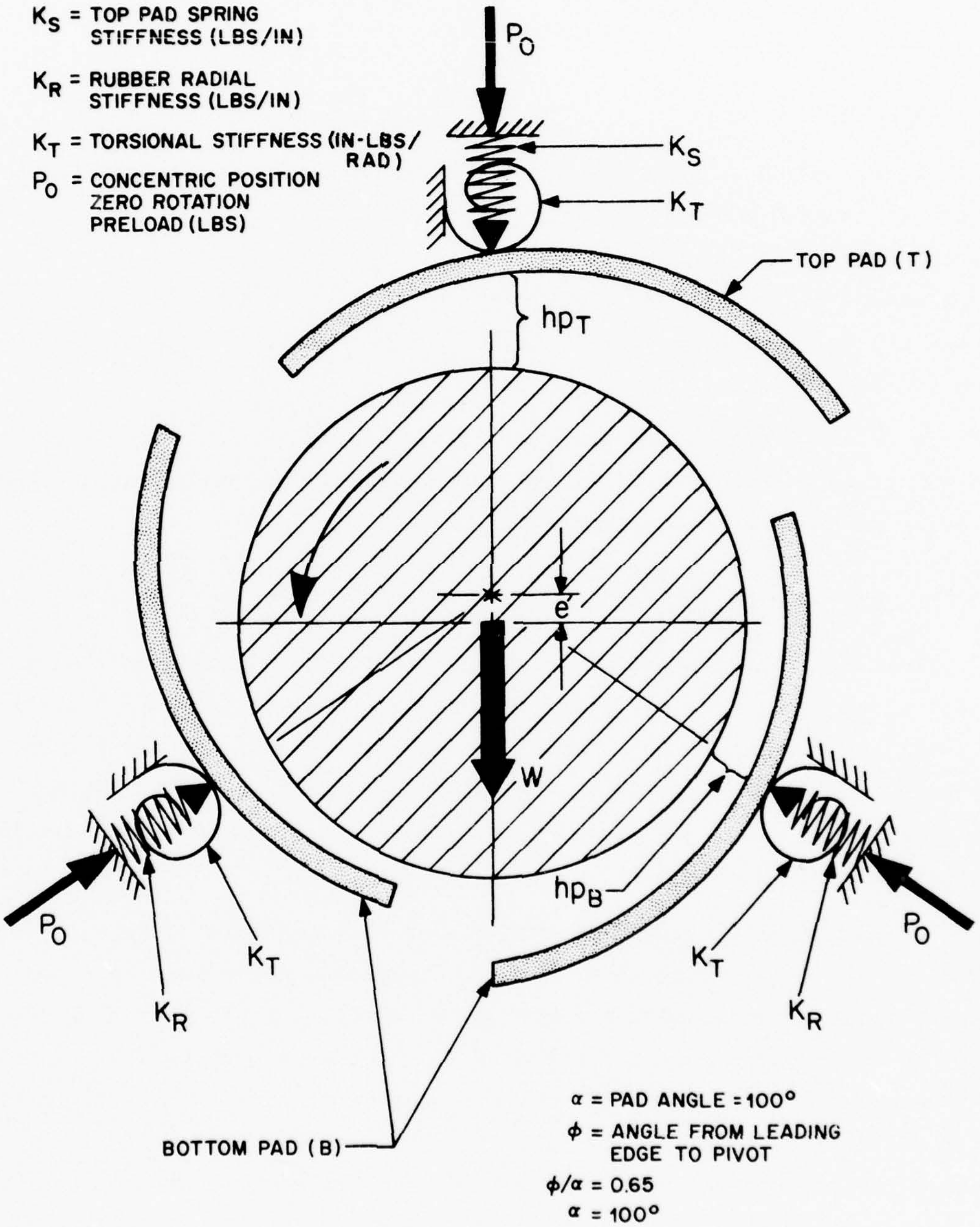

Figure 3-1. Mathematical Model of Compliant-Pivot Bearing

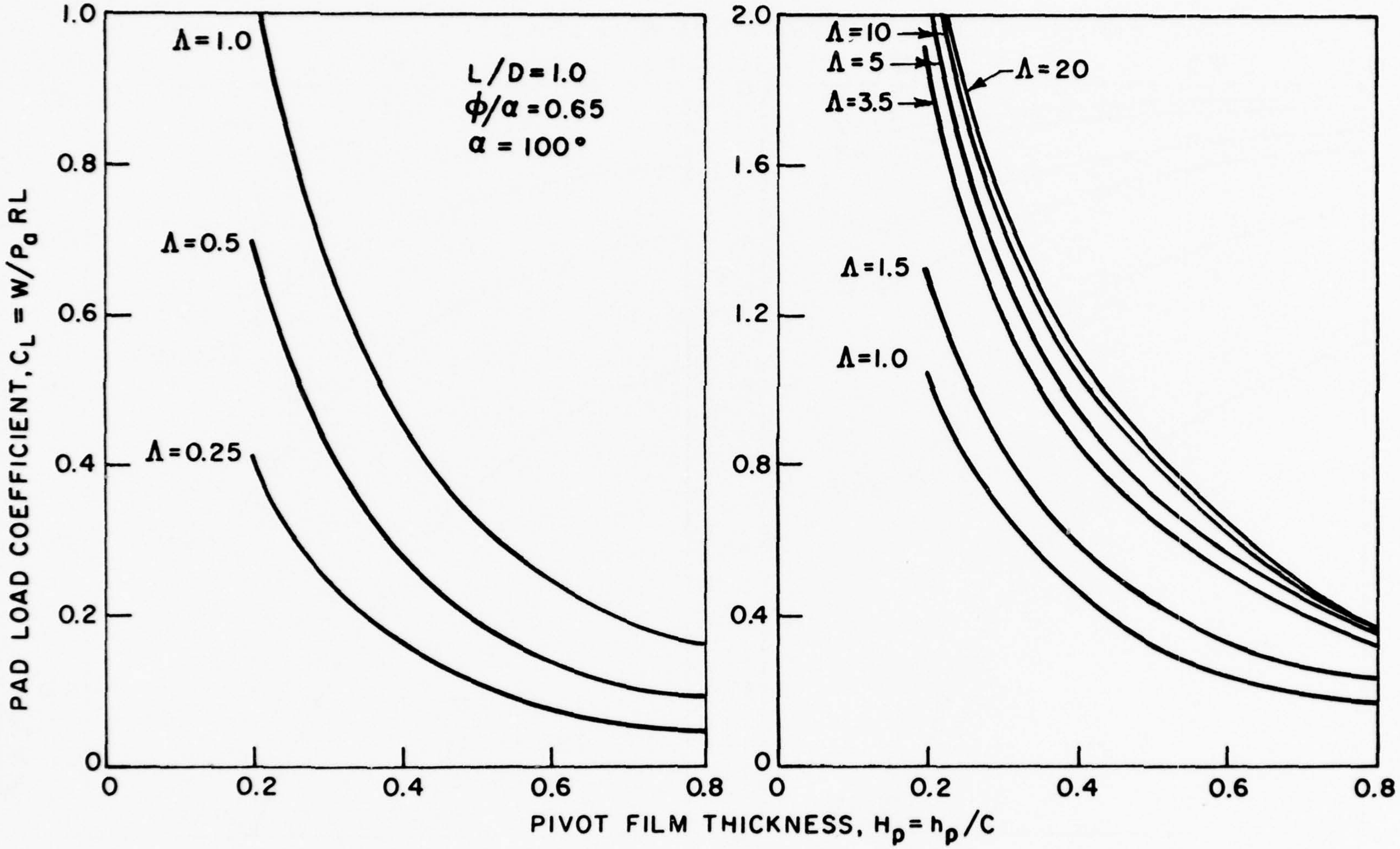

Figure 3-2. Fluid-Film, Pad Load Coefficient vs. Pivot Film Thickness

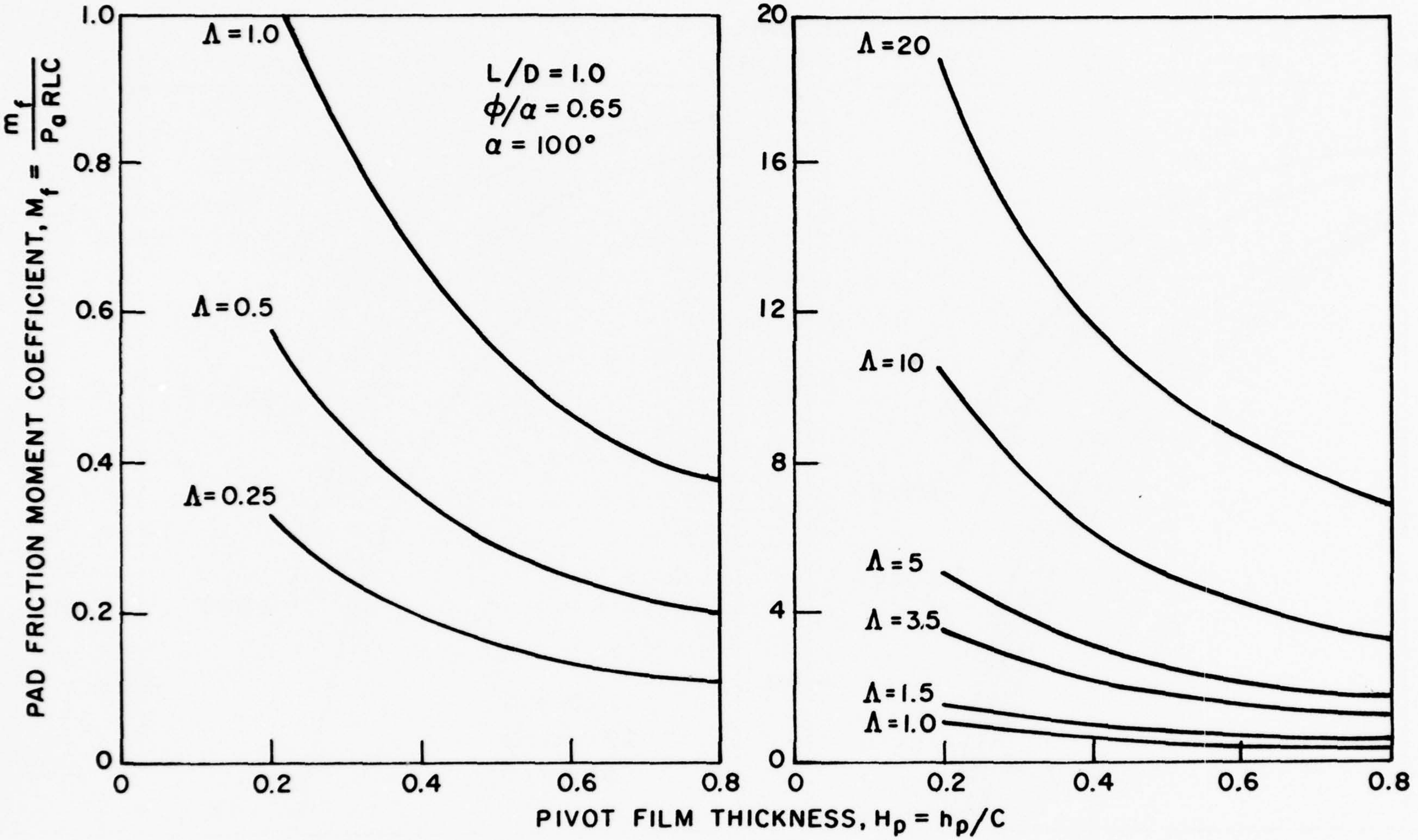

Figure 3-3. Fluid-Film, Pad Friction Moment Coefficient vs. Pivot Film Thickness

since they emanate from the origin. The extrapolated curves are shown on Figures 3-4 and 3-5.

There are two values of the compressibility parameter Λ that are of interest. These are a Λ value of .368 which corresponds to the cold clearance condition (radial clearance, C = .0032) and a shaft operating speed of 60,000 rpm, and a Λ value of 1.5 (C = .00159) which is the optimum value for load capacity. To obtain data at the intermediate value of $\Lambda = 0.368$, a direct ratio was applied to the $\Lambda = 0.5$ information.

By conversion of the non-dimensional data, fluid-film performance can be obtained. Tabulations of single-pad load capacity vs. pivot film thickness are shown on Table II.

Plots of bearing load capacity vs. pivot film thickness are shown on Figure 3-6. Note that there is no significant difference between the pad loads for the two different compressibility parameters. Only a slight advantage is gained from the $\Lambda = 1.5$ situation. Therefore, with respect to load capacity, reference can be made to a single set of theoretical load data, rather than distinguishing between two values of Λ.

Individual pad power losses were computed in a similar manner and are tabulated in Table III.

Power loss curves are shown on Figure 3-7. As with the load data, there is no marked difference in power loss as a function of the compressibility parameter Λ.

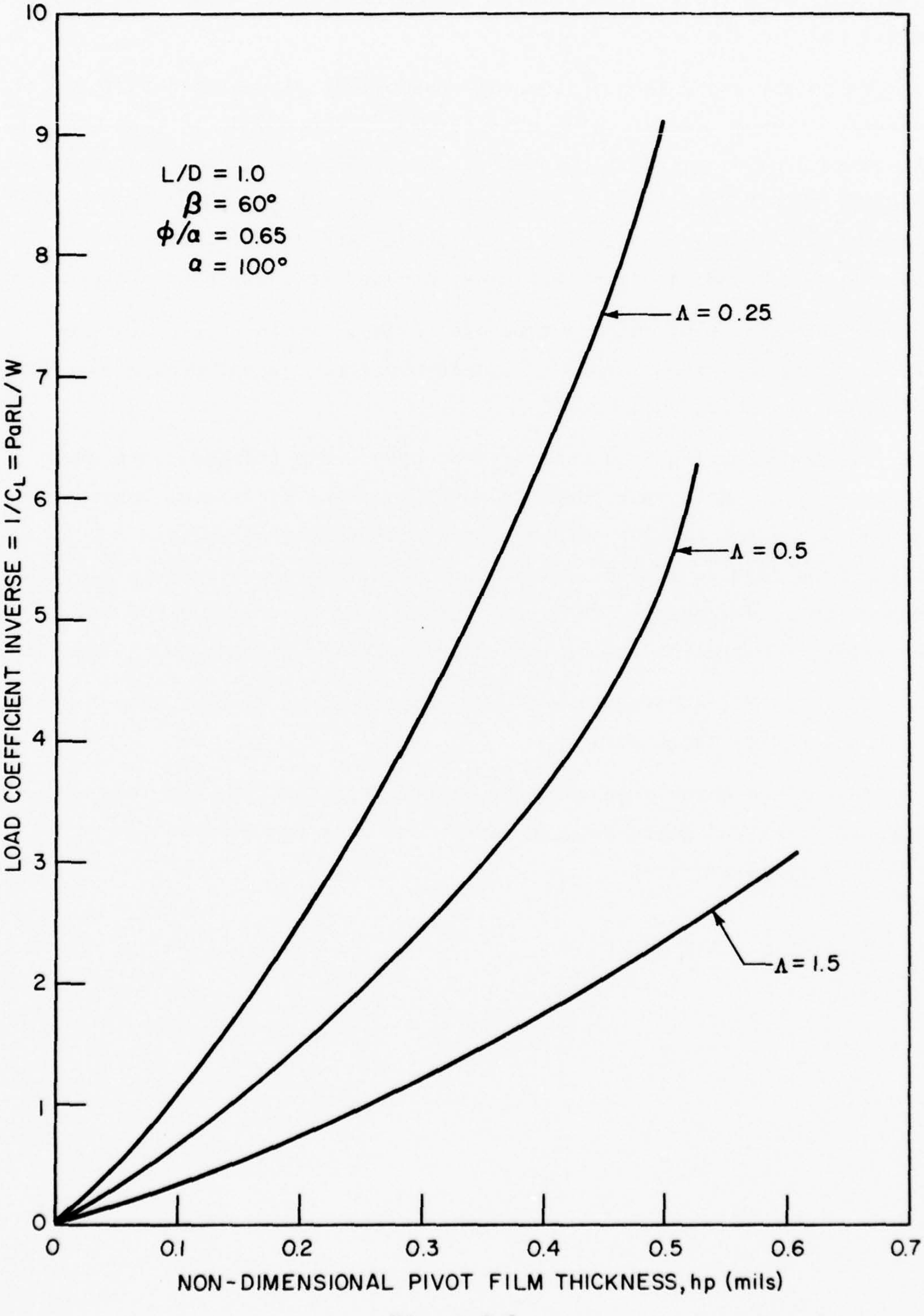

10
9
8
7
6
5
4
3
2
1
0
0
0.1
0.2
0.3
0.4
0.5
0.6
0.7
LOAD COEFFICIENT INVERSE = $1/C_L$ = PaRL/W
NON-DIMENSIONAL PIVOT FILM THICKNESS, hp (mils)
L/D = 1.0
β = 60°
ϕ/α = 0.65
α = 100°
Λ = 0.25
Λ = 0.5
Λ = 1.5

Figure 3-4

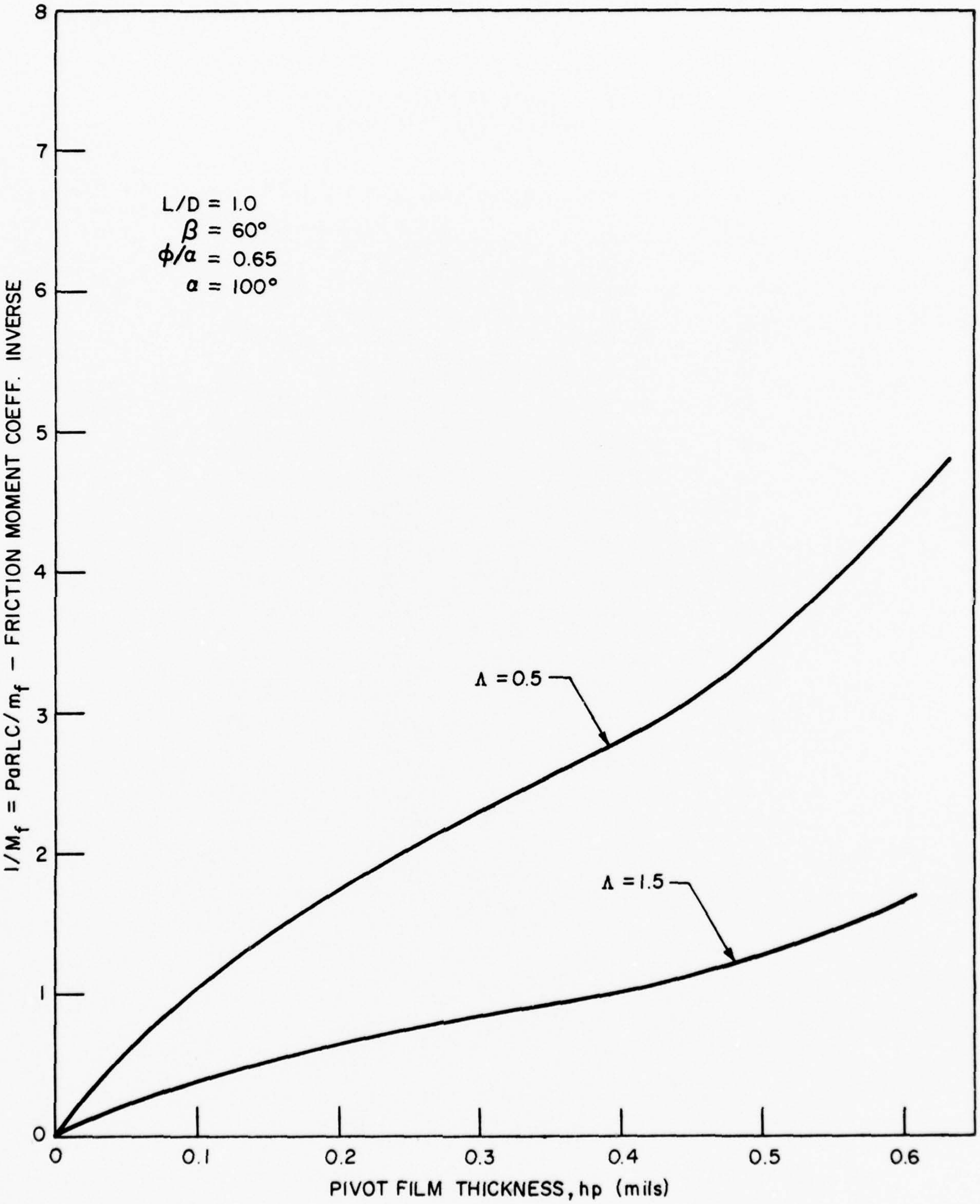
L/D = 1.0
β = 60°
ϕ/α = 0.65
α = 100°
Λ = 0.5
Λ = 1.5
$1/M_f = PaRLC/m_f$ – FRICTION MOMENT COEFF. INVERSE
PIVOT FILM THICKNESS, hp (mils)
0
1
2
3
4
5
6
7
8
0.1
0.2
0.3
0.4
0.5
0.6

Figure 3-5

Table II. Single Pad Load Capacity vs. Pivot Film Thickness

L = 1.4 in.; D = 1.4 in.; N = 60,000 rpm; $\mu = 3 \times 10^{-9}$ lb-sec/in^2

$\Lambda = .368$, C = .0032		$\Lambda = 1.5$, C = .00159	
h_p mils	W lbs	h_p mils	W lbs
.08	70.72	.0795	96.04
.16	35.36	.159	48.02
.32	16.32	.239	26.19
.48	10.10	.318	19.21
.64	7.32	.398	15.16
.80	5.52	.478	12.01
.96	4.51	.557	9.94
1.12	3.59	.636	8.23
1.28	2.95	.716	7.03
1.44	2.44	.795	6.13
1.60	2.02	.875	5.44
1.92	1.48	.954	4.80
2.24	1.06	1.113	3.74
2.56	.955	1.272	3.17
		1.59	1.73

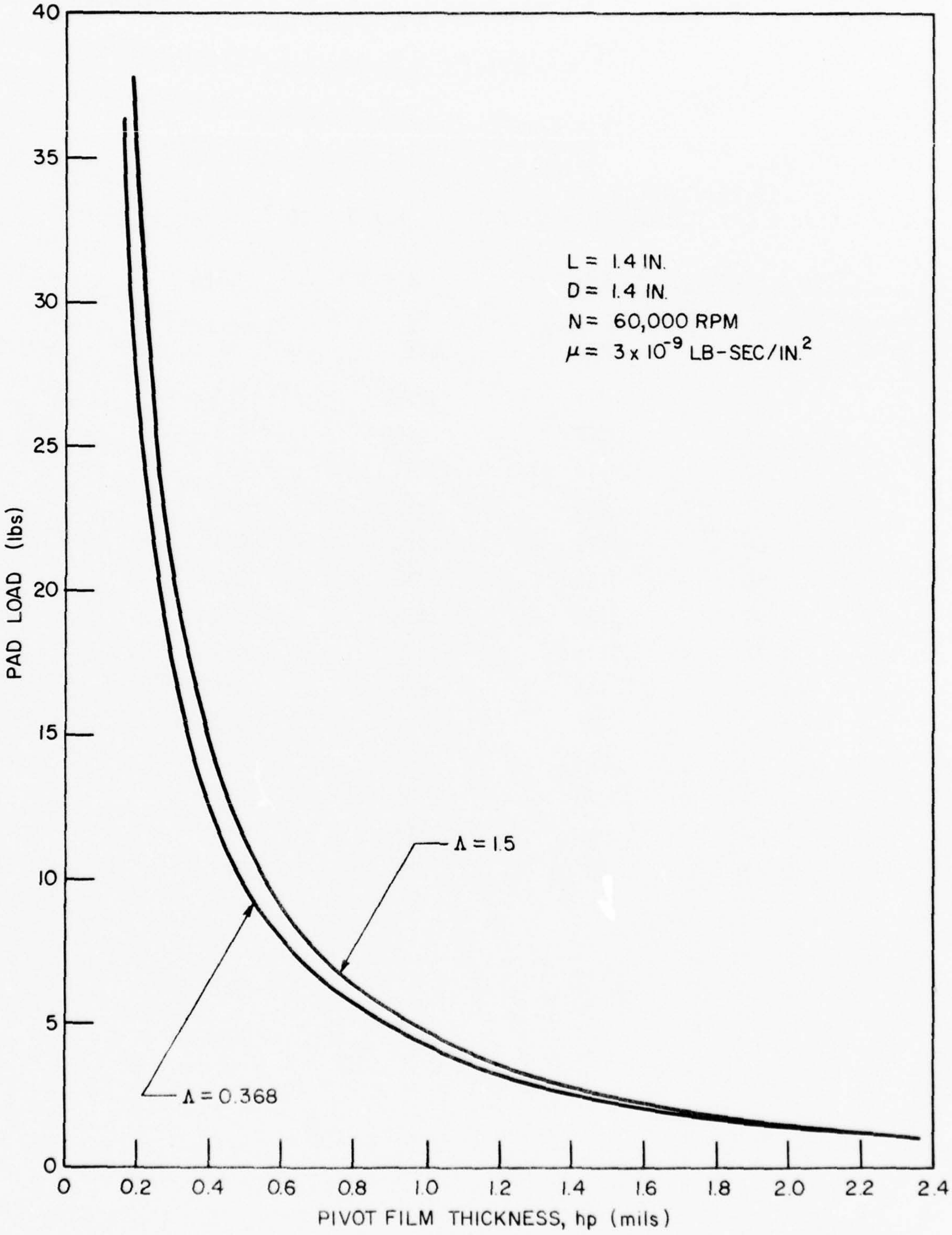
40
35
30
25
20
15
10
5
0
PAD LOAD (lbs)
0
0.2
0.4
0.6
0.8
1.0
1.2
1.4
1.6
1.8
2.0
2.2
2.4
PIVOT FILM THICKNESS, hp (mils)
L = 1.4 IN.
D = 1.4 IN.
N = 60,000 RPM
μ = 3 x 10⁻⁹ LB-SEC/IN.²
Λ = 1.5
Λ = 0.368

Figure 3-6

Table III. Single Pad Power Loss vs. Pivot Film Thickness

L = 1.4 in., D = 1.4 in., N = 60,000 rpm, $\mu = 3 \times 10^{-9}$ lb-sec/in^2

$\Lambda = .368$, C = .0032		$\Lambda = 1.5$, C = .00159	
h_p mils	Power Loss HP	h_p mils	Power Loss HP
.08	.1077	.0398	.218
.16	.0557	.0795	.109
.32	.0314	.159	.058
.48	.0230	.239	.042
.64	.0190	.318	.034
.80	.0160	.398	.029
.96	.0140	.477	.026
1.12	.0125	.557	.024
1.28	.0116	.636	.0211
1.44	.0105	.716	.0189
1.60	.0094	.795	.017
1.92	.0073	.954	.017
2.24	.0068	1.113	.013
2.56	.0064	1.272	.013

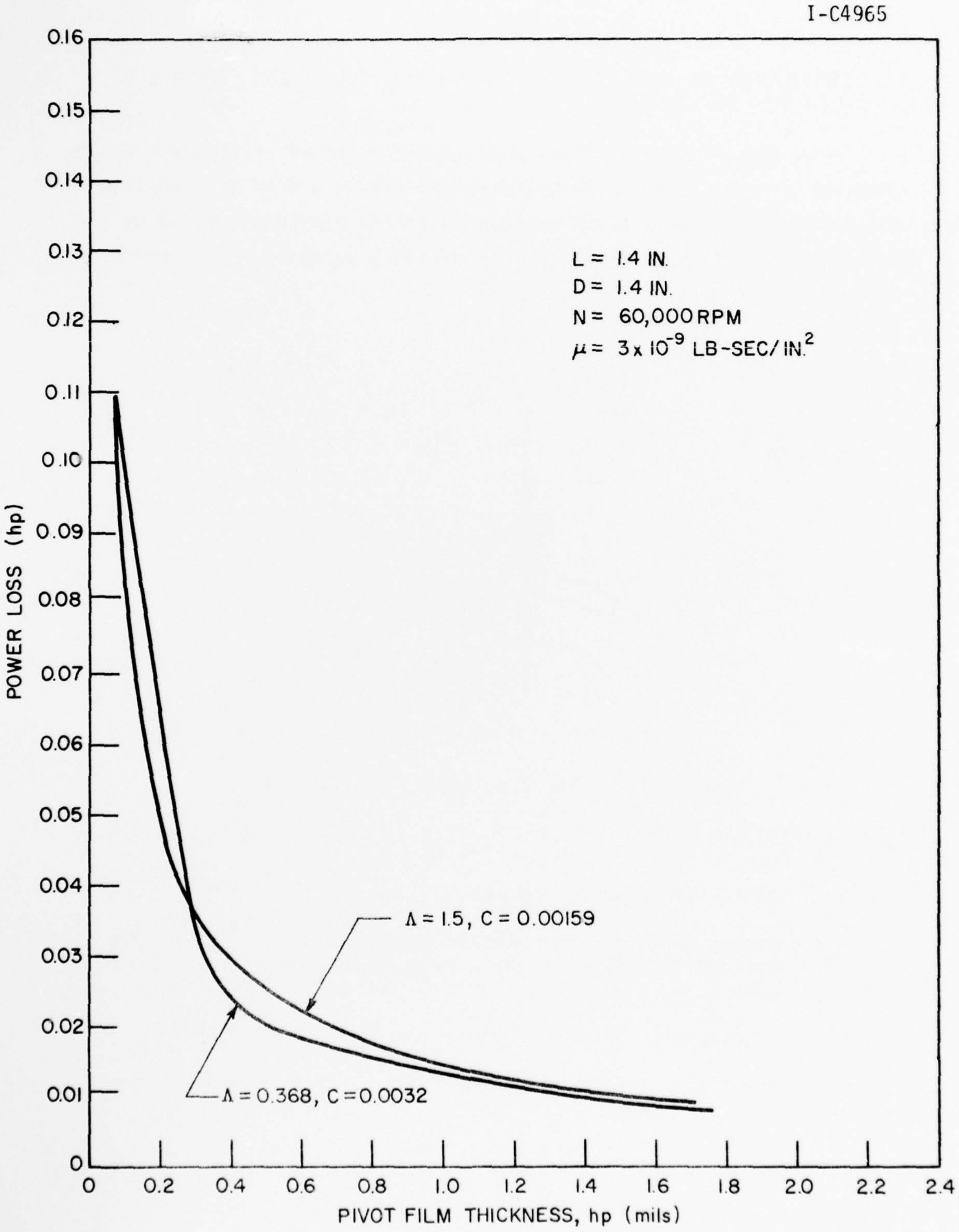
I-C4965
L = 1.4 IN.
D = 1.4 IN.
N = 60,000 RPM
μ = 3 x 10⁻⁹ LB-SEC/IN.²
Λ = 1.5, C = 0.00159
Λ = 0.368, C = 0.0032
POWER LOSS (hp)
PIVOT FILM THICKNESS, hp (mils)
0
0.01
0.02
0.03
0.04
0.05
0.06
0.07
0.08
0.09
0.10
0.11
0.12
0.13
0.14
0.15
0.16
0.2
0.4
0.6
0.8
1.0
1.2
1.4
1.6
1.8
2.0
2.2
2.4

Figure 3-7

3.3 COMPUTATION OF LOAD CAPACITY VS. SHAFT DISPLACEMENT FROM THE DEAD REST POSITION

There are various reference positions from which performance can be computed. In the test program, the system was in a dead rest position with gravity load on the bearing and a specific pre-load applied by the beam spring. This was chosen as the reference position. The theoretical development proceeds as follows:

Top Pad

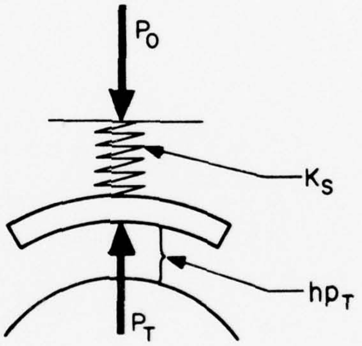

Figure 3-8. Top Pad, Radial Equilibrium

$$P_T = K_S \; (e' + h_{p_T}) + P_o \qquad (1)$$

P_T = Fluid-film load of top pad

P_o = Spring preload of top pad in the dead rest position. The symmetric geometry results in equally applied preload to all pads

e' = Displacement of shaft towards the top pad

h_{p_T} = pivot film thickness of top pad

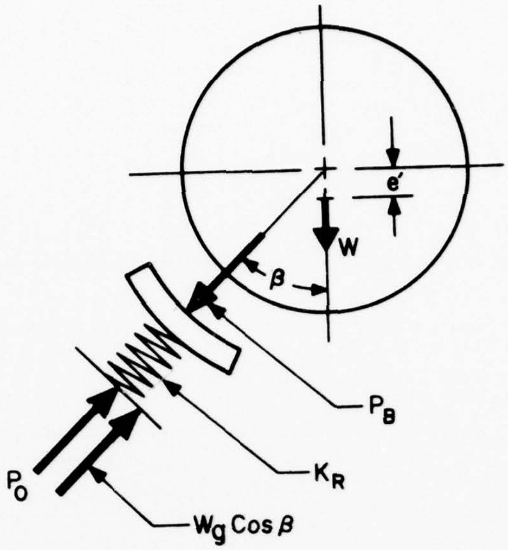

Figure 3-9. Bottom Pad, Radial Equilibrium

Bottom Pad (see Figure 3-9)

$$P_B = P_o - K_R e' \cos \beta + K_R h_{p_B} + W_g \cos \beta \qquad (2)$$

P_B = Fluid-film force on bottom pad

K_R = Elastomer radial stiffness on bottom pads

W_g = Gravity load of shaft

h_{p_B} = Pivot film thickness of bottom pads

For any value of e' (the displacement from the dead rest position) the loads P_B and P_T can be computed as a function of their respective pivot film thicknesses.

The intersection of the curves generated by equations (1) and (2) with the fluid film curves of pad load vs. pivot film thickness (Figure 3-6) will establish the appropriate pad loads and pivot film thicknesses as a function of the displacement from the dead rest position e'.

The total external load carried by the journal is

$$W = P_B - P_T \qquad (3)$$

This computational procedure was followed for three different values of elastomer spring stiffness and initial pre-load. Results are plotted on Figure 3-10. For heavy loading, the displacement of the journal from the dead-rest position is downward (e' negative) for all three values of the elastomer stiffness. For infinite elastomer stiffness, the displacement would

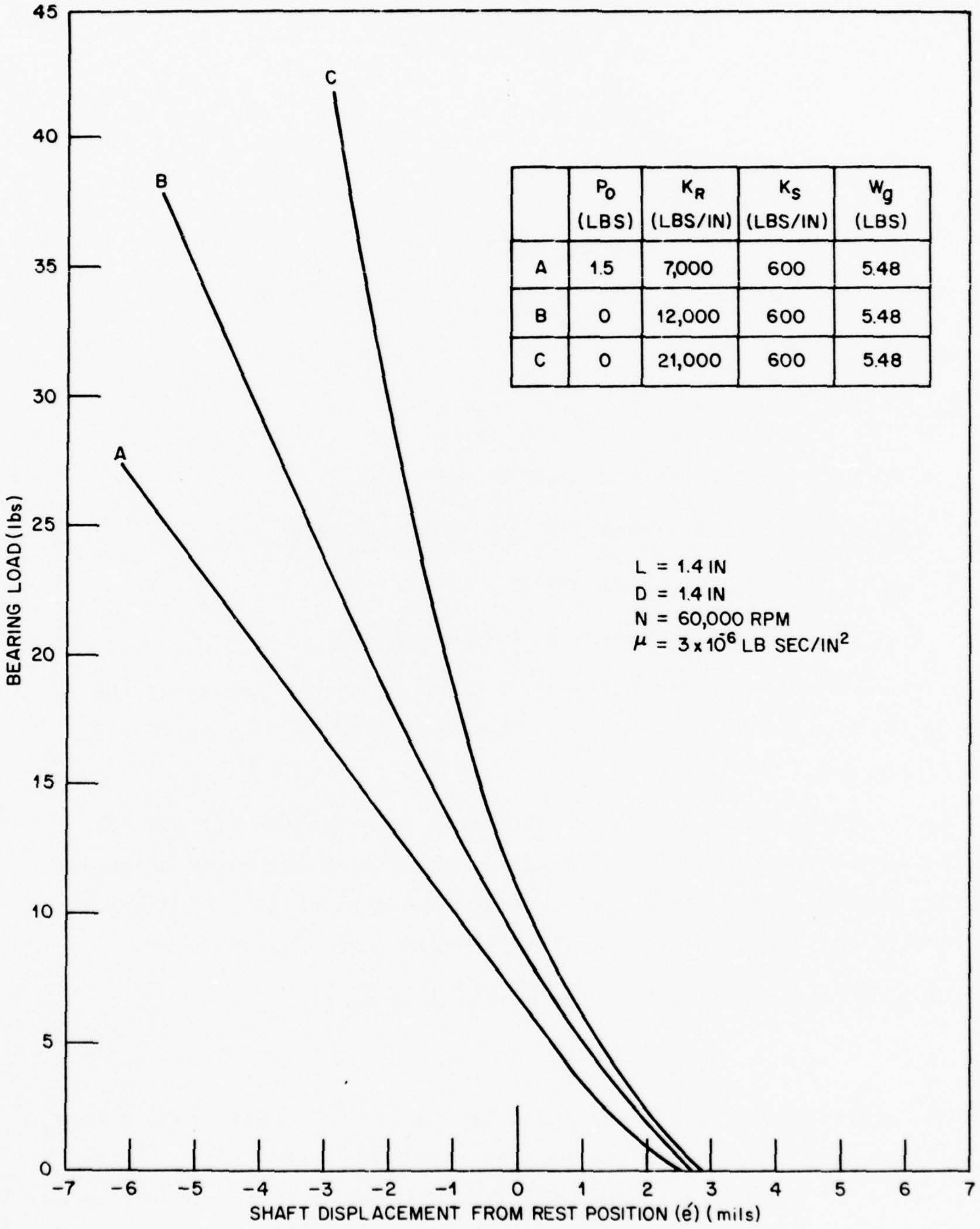

	P_0 (LBS)	K_R (LBS/IN)	K_S (LBS/IN)	W_g (LBS)
A	1.5	7,000	600	5.48
B	0	12,000	600	5.48
C	0	21,000	600	5.48

Figure 3-10

always be positive or upward. From the theoretical curves, the computed values of bearing stiffness can be obtained by computing the slopes of the individual curves. The bearing stiffnesses K_B, in the high load region, are tabulated below:

P_o (lbs)	K_R (lbs/in)	K_S (lbs/in)	K_B (lbs/in)
1.5	7,000	600	3,250
0	12,000	600	5,250
0	21,000	600	9,900

Thus, the bearing stiffness is considerably altered by the stiffness of the elastomer and to a lesser degree by the pre-load.

Bearing load as a function of the loaded pad pivot film thickness is shown on Figure 3-11. Curves are shown for three values of pre-load and elastomer stiffness. At the high load condition all curves converge to the same value of loaded pad, pivot film thickness.

3.4 BEARING POWER LOSS

Overall bearing power loss was estimated from the individual pad power loss information, Figure 3-7. It was determined by summing the individual contributions of each pad as a function of its pivot film thickness. Results are shown on Figure 3-12. A slight advantage is gained from the larger clearance bearing, but as the case with load capacity, the differences are not significant. At high load conditions, when pivot film-thickness becomes small the overall power loss substantially increases.

3.5 ANALYSIS OF COMPLIANT MOUNTS

Calculations of mount stiffnesses were accomplished by using approximate formulae derived for bonded rubber blocks [4]. Let K_R and K_A denote the radial and angular stiffness. They can be expressed in

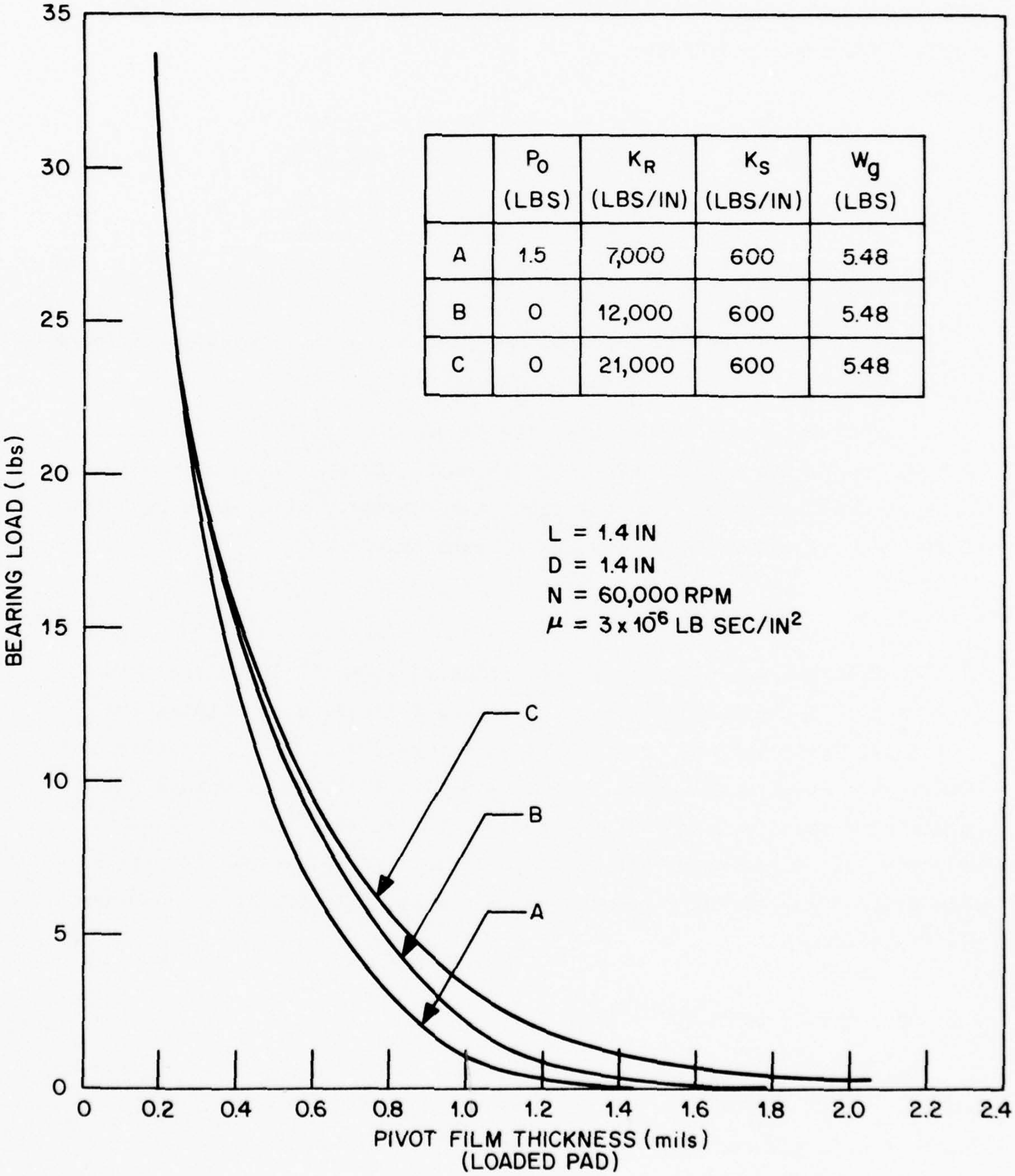

	P_O (LBS)	K_R (LBS/IN)	K_S (LBS/IN)	W_g (LBS)
A	1.5	7,000	600	5.48
B	0	12,000	600	5.48
C	0	21,000	600	5.48

L = 1.4 IN
D = 1.4 IN
N = 60,000 RPM
$\mu = 3 \times 10^{-6}$ LB SEC/IN^2

Figure 3-11

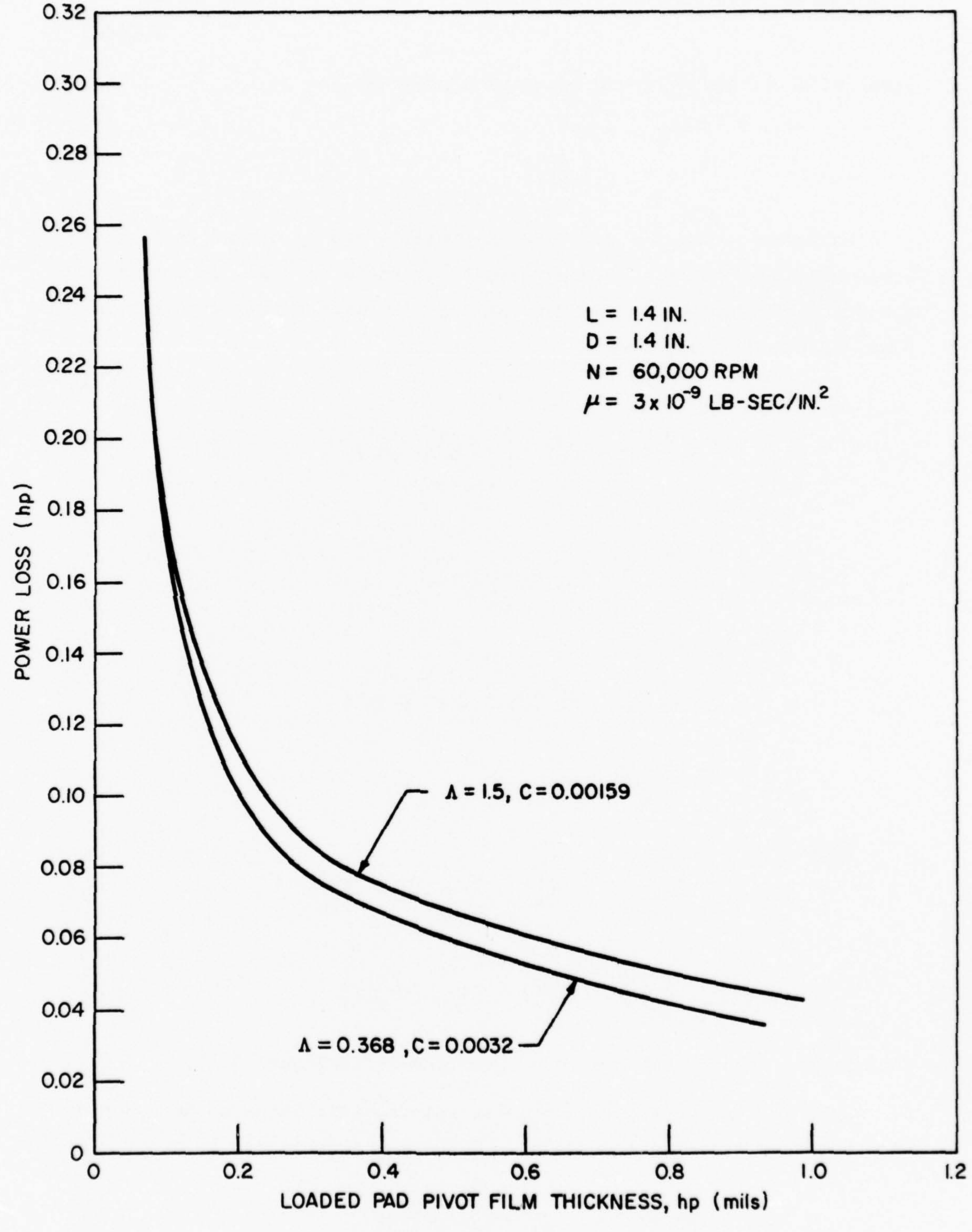
0.32
0.30
0.28
0.26
0.24
0.22
0.20
0.18
0.16
0.14
0.12
0.10
0.08
0.06
0.04
0.02
0
POWER LOSS (hp)
0
0.2
0.4
0.6
0.8
1.0
1.2
LOADED PAD PIVOT FILM THICKNESS, hp (mils)
L = 1.4 IN.
D = 1.4 IN.
N = 60,000 RPM
μ = 3 x 10⁻⁹ LB-SEC/IN.²
Λ = 1.5, C = 0.00159
Λ = 0.368 , C = 0.0032

Figure 3-12

terms of mount geometry and material properties as

$$K_R = f_c AE/\ell$$
$$K_A = f_b AK^2 E/\ell \qquad (4)$$

Expressions for the numerical factors f_c and f_b depend on the cross-sectional shape. When a rectangular block of sides 2a and 2b is subjected to compression and bending about an axis parallel to the 2b side, f_c can be written as

$$f_c = f_{c1} + f_{c2} \qquad (5)$$
$$f_{c1} = \frac{4}{3} - \frac{2}{3}(ab + h^2)/(a^2 + b^2 + 2h^2)$$
$$f_{c2} = \frac{1}{3}\frac{(2a)^2}{h^2} g_1$$

and

$$f_b = f_{b1} + f_{b2} \qquad (6)$$
$$f_{b1} = \frac{4}{3} - \frac{2}{3}(ab + 4h^2)/(a^2 + b^2 + 8h^2)$$
$$f_{b2} = \frac{6}{\pi^4}\frac{(2a)^2}{h^2} g_2$$

where

$$g_1 = 1 - \frac{192}{\pi^5}\frac{a}{b}\sum_{n=1,3,5}\frac{1}{n}\,5 \tan h \left(\frac{n\pi b}{2a}\right) \qquad (7)$$

$$g_2 = \sum_{n=1}\frac{1}{n^4}\left[1 - \left(\frac{n\pi b}{a}\right)^{-1} \tan h \left(\frac{n\pi b}{a}\right)\right]$$

Constants g_1 and g_2 are presented graphically in Figure 3-13.

Gent [4] has developed a precise relationship between the indentation hardness and elastic modulus. This relationship may be written as

$$E\ (\mathrm{kg/cm^2}) = \frac{56 + 7.66S}{2.67r\ (254-2.54S)} \qquad (8)$$

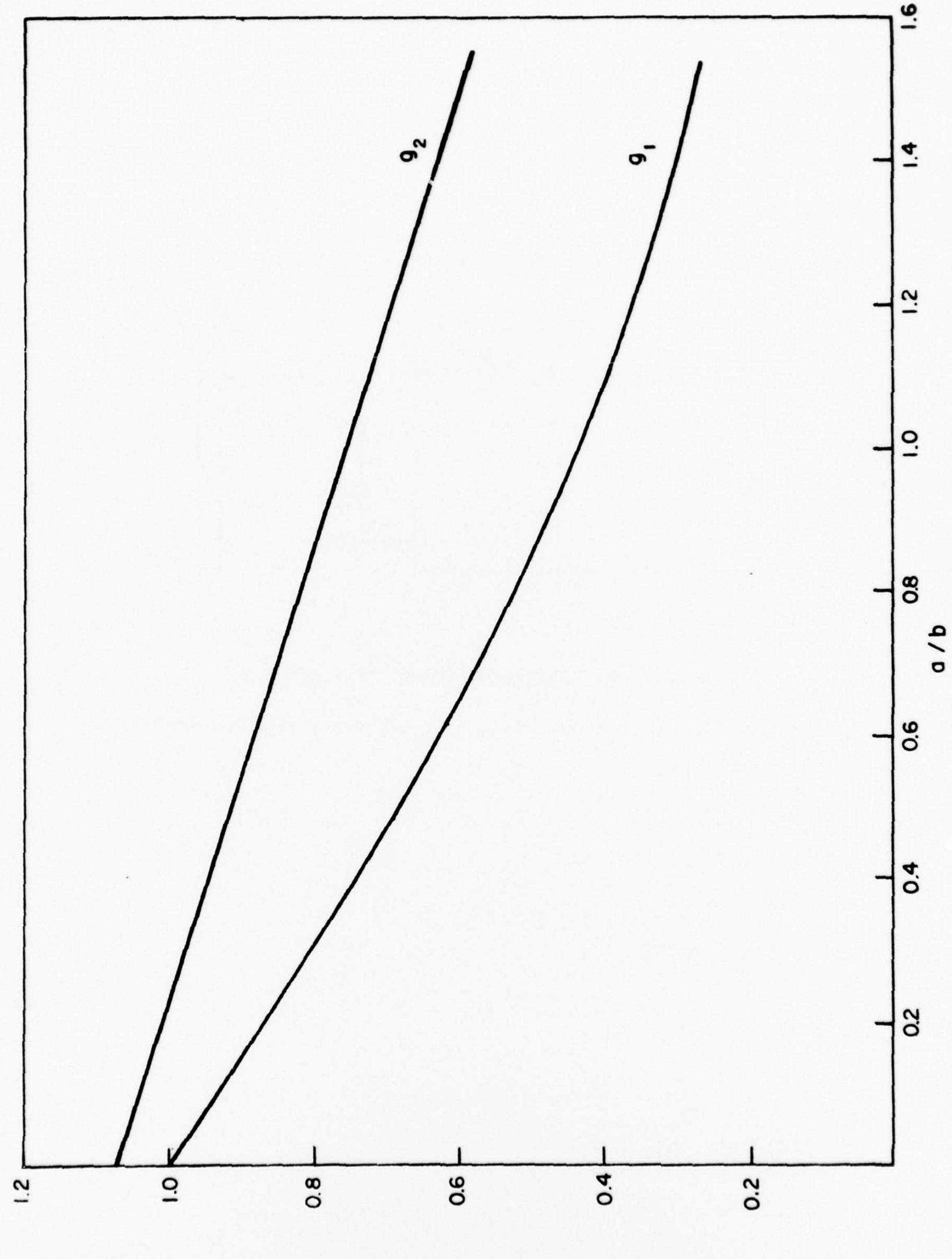

Figure 3-13. Stiffness Factors for Rectangular Rubber Blocks

where

E = Young's modulus

S = Hardness (A)

r = Radius of indentor = .0515 cm

The elastomer mounts for the loaded pads has the following configuration:

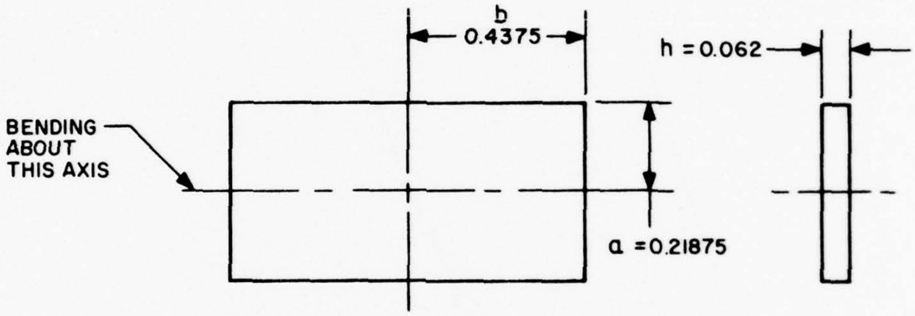

Figure 3-14. Elastomer Pivot Configuration

Applying the foregoing formulas, the following results have been computed:

$f_{c1} = 1.06459$

$f_{c2} = 11.618$

$f_{c} = 12.683$

$E = 296.43 \text{ lbs/in}$

$\boxed{K_R = 23{,}210 \text{ lbs/in}}$

$f_{b1} = 1.00675$

$f_{b2} = 2.76$

$f_{b} = 3.767$

$K^2 = .01596 \text{ in}^2$

$\boxed{K_B = 109.47 \text{ in-lb/rad}}$

The computed value of radial stiffness is slightly higher than the measured value as indicated on Table I, and the computed value of bending stiffness is slightly lower than measured. The variations could be due to the approximations in the theory or experimental error. Small displacement measurements are difficult to obtain without sophisticated instrumentation and are not readily repeatable.

There is some evidence that suggests that the theoretical value is closer to reality. In the testing program, to be subsequently discussed, actual displacements from the dead-rest position were always positive (upward). As shown on Figure 3-10, even with an elastomer stiffness of 21,000 lbs/in, under high loading, shaft displacements are negative (downward). This indicates that actual elastomer stiffness is higher than 21,000 lbs/in which is greater than the measured value of 18,000 lbs/in. Under high loading, non-linearities in the rubber characteristics probably introduce significant stiffness increases above those presumed to occur.

3.6 BEARING STABILITY

High speed tilting-pad bearing systems may be subject to two types of instabilities. The first is rotor whirl because the pitch resistances or inertias of the pads are excessive, introducing a lag in the pitch motions of the pads. The second is pad flutter due to improper inertia characteristics and insufficient damping in the pivot. Information exists [5] that enables pad inertias to be selected to avoid both flutter and whirl problems provided pivot resistance is negligible. Using information from reference [5], a stability map was generated and is shown on Figure 3-15. It is a plot of the pad pitch inertia coefficient $\overline{I}_p$ vs. the shaft mass coefficient $\overline{M}_s$. $\overline{I}_p$ is a parameter related to the pad pitch inertia, and $\overline{M}_s$ is a parameter relating to the quantity of mass that the bearing supports. The stability limit is shown by the dashed line. The actual performance of the bearing is shown by the solid line. The only variable that is changing is the shaft speed Ω, thus the curve represents the effects of speed on stability. The actual shaft speed is shown on the upper portion of the graph. The curve indicates that the new design is stable over the operating range of the machine. The stability information was generated for the large (1.8 in. dia.) bearing since its stability characteristics are inferior to the smaller bearing.

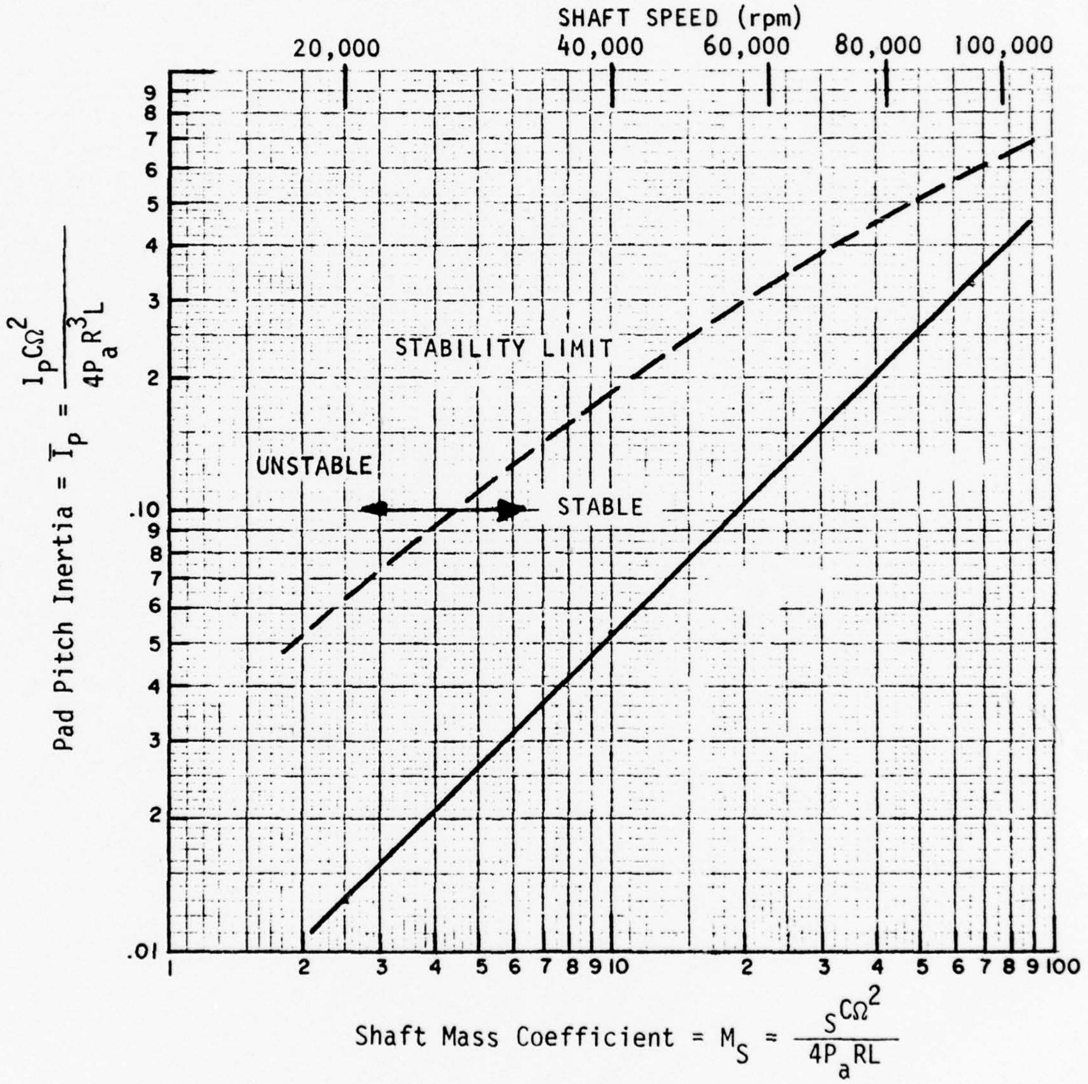

Figure 3-15. Stability Map, Compliant-Mounted Journal Bearing, Inboard Bearing

4. EXPERIMENTAL PROGRAM

4.1 DESCRIPTION OF TEST RIG AND INSTRUMENTATION

Figure 4-1 is a schematic of the FIRL high speed test rig. The rig basically consists of a base plate, two bearing pedestals, the rotor with integral turbine and the nozzle assembly. The test bearings are inserted in the pedestals. The rotor was slightly tilted towards the inboard end bearing so that a light load would be imposed upon the thrust bearing.

The rotor was driven by a four-nozzle impulse turbine, which consisted of the nozzle ring and turbine buckets machined into the rotor. The rig was designed for easy access to the bearings and provided for insertion of extensive instrumentation. Figure 4-1 indicates the instrumentation applied to the rig. Close-up photographs of the test rig are shown on Figures 4-2 and 4-3.

Figure 4-4 is a photograph of the compliant-mounted test rig arrangement and instrumentation. Inductance probes were used to monitor shaft motions at each bearing pedestal location. Two probes were mounted at each location 90 degrees apart. Two probes at each bearing pedestal were also installed to monitor the leading and trailing edges of the most heavily loaded shoe. A photocell monitored shaft rotational speed. Thermocouples were embedded into the tilting pads and were used to establish pad temperatures and housing temperatures. Thermocouple readings were printed at prespecified intervals by a digital recorder. Oscilloscopes monitored shaft vibrations and absolute displacements. All information was recorded on a 14-channel tape recorder for subsequent playback and interpretation. Figure 4-5 shows the test rig modified for load testing. A Kapton (DuPont product) foil bearing was employed for transmitting dead weight loads to the shaft. The test rotor was balanced to 0.0003 in-oz.

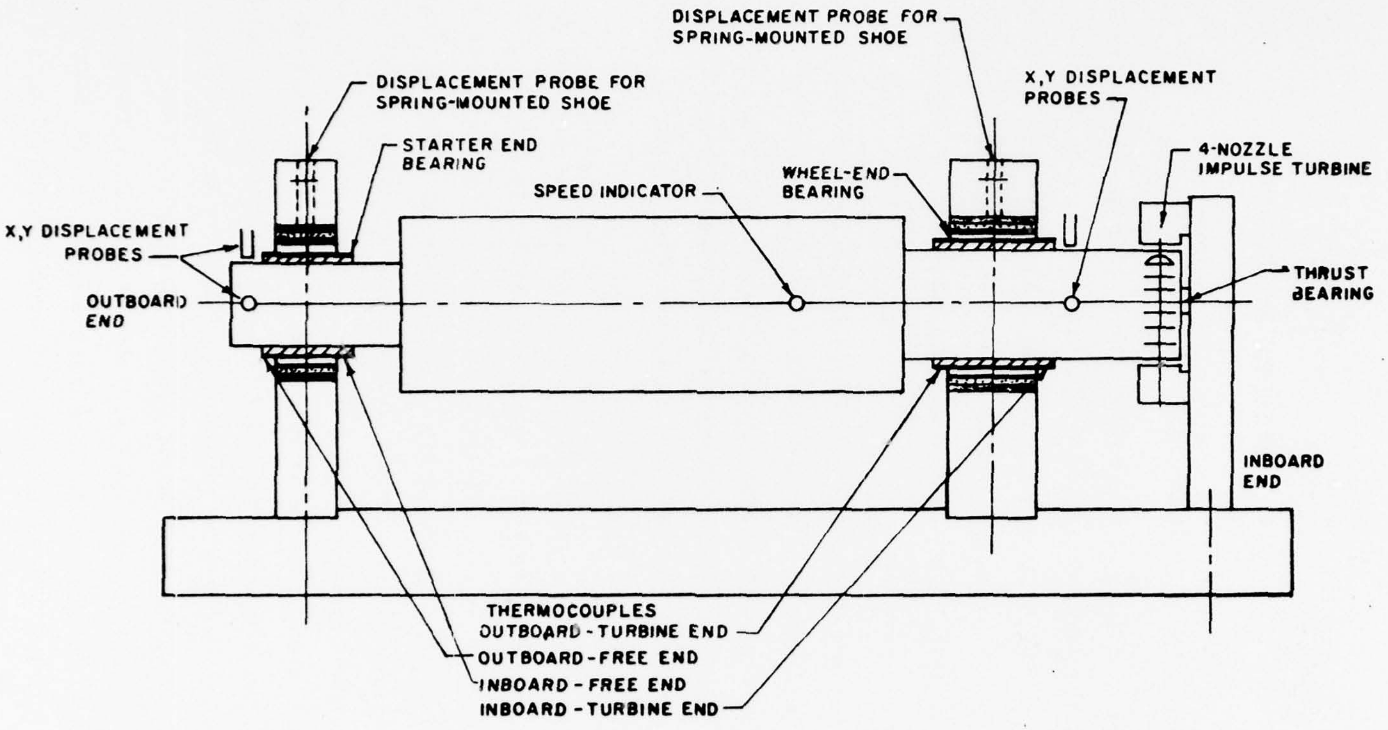

I-C4965

Figure 4-1. Schematic of High-Speed Gas Bearing Test Rig

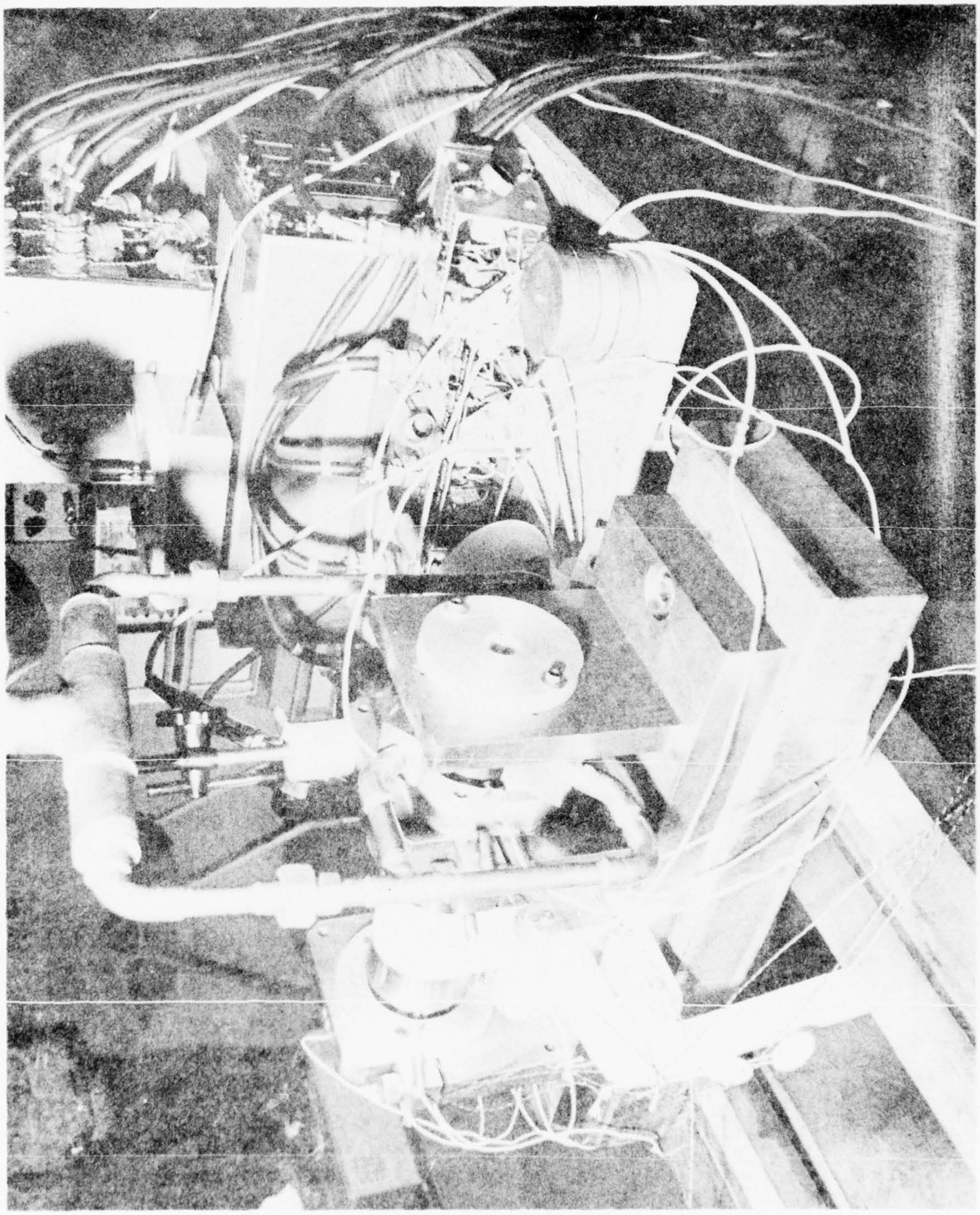

Figure 4-2. Close-up of High-Speed, Gas Bearing, Component Test Rig

I-C4965

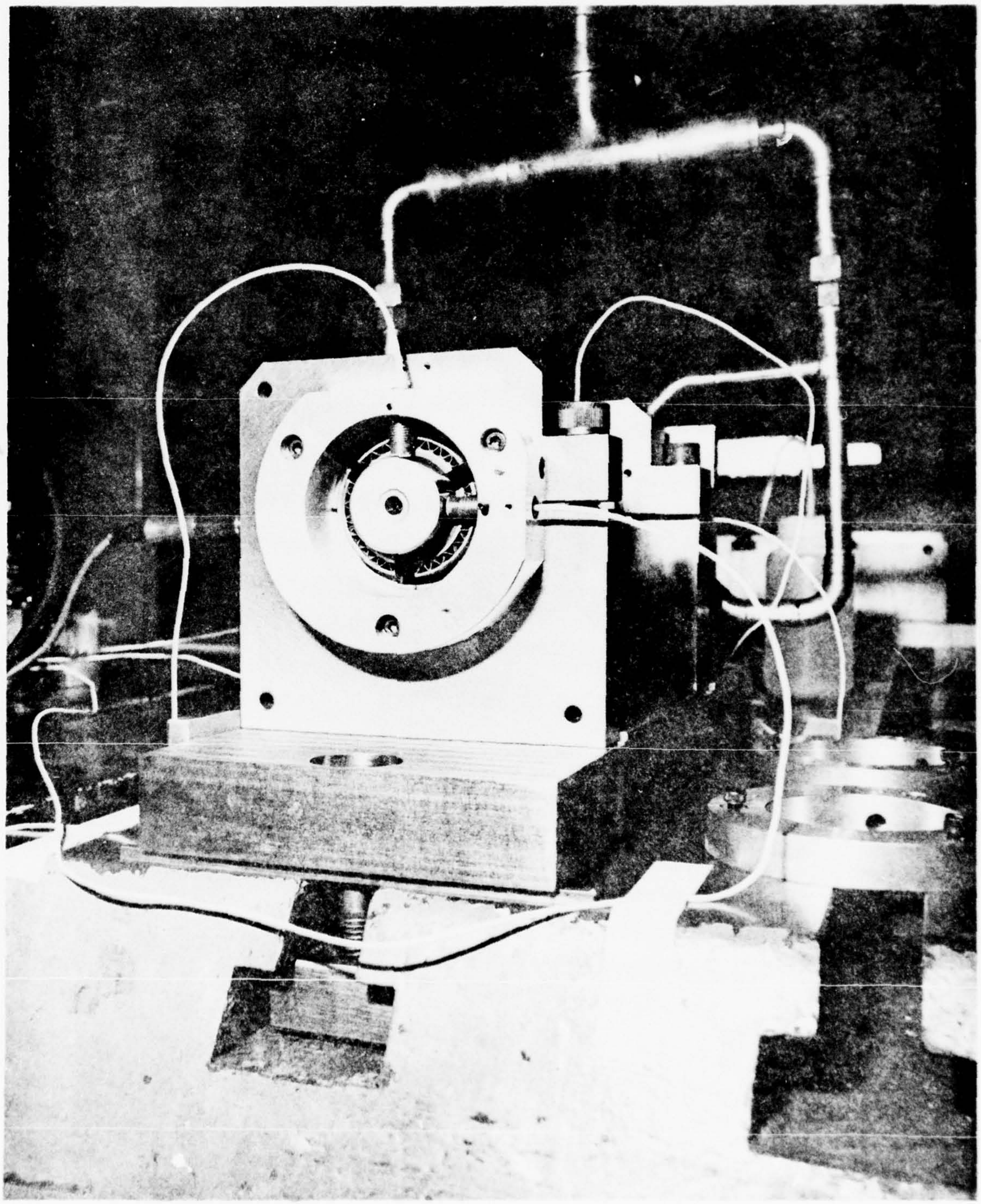

Figure 4-3. Journal Bearing Installation, High-Speed, Gas-Bearing Component Test Rig

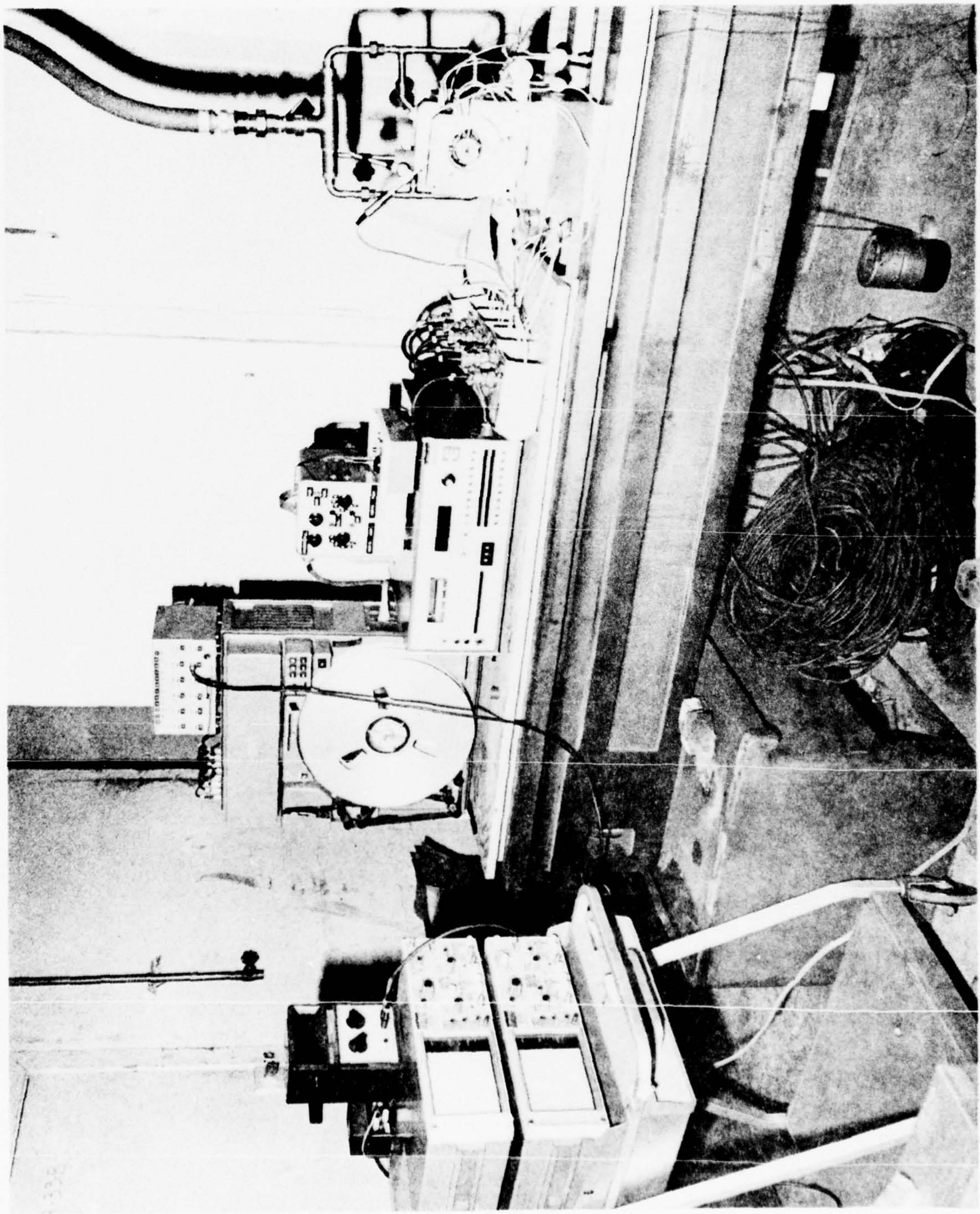

Figure 4-4. Compliant-Mounted Bearing Test Rig and Instrumentation

I-C4965

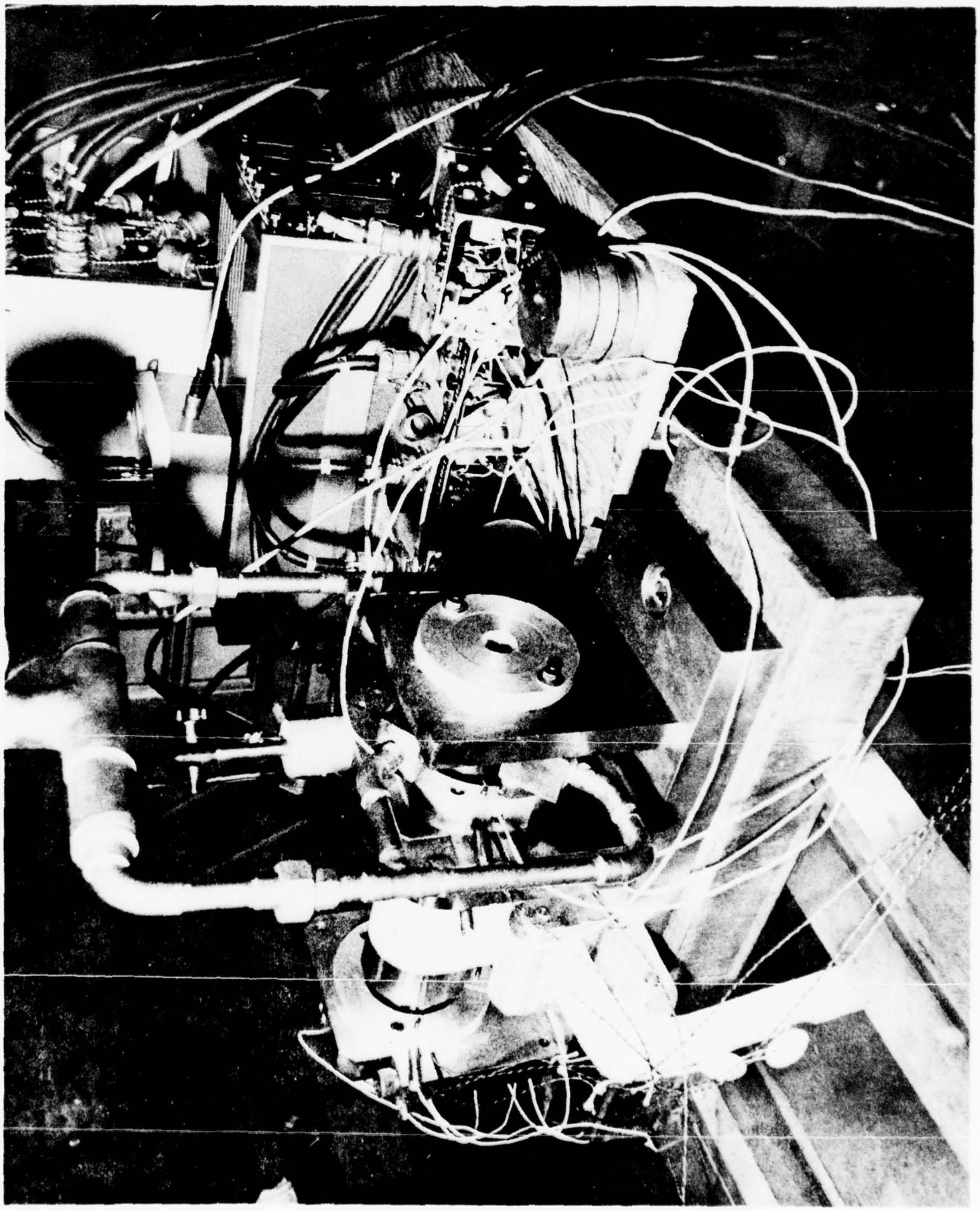

Figure 4-5. Compliant-Mounted Bearing, High-Speed Rig with Foil Bearing for Load Transmittal

4.2 HIGH SPEED TESTING

In July, 1976, tests were conducted which were representative of high-speed test results. The maximum operating speed obtainable with the test apparatus was 76,000 rpm, and this was the speed at which the tests were conducted. Figure 4-6 illustrates orbit plots of both ends of the rotor. Peak to peak amplitudes were approximately 0.6 mils at both ends. Figures 4-7 and 4-8 are frequency plots which indicate relative amplitude as a function of the frequency present in the system. The predominant frequency occurs at the running speed. There is a frequency (Figure 4-8) that fluctuated between 45,000 cpm and 65,000 cpm. It had a relatively low amplitude and was related to the impulse turbine (throttling the turbine at operating speed removed this frequency). The bearings remained stable and the orbit levels remained the same throughout the test. There was no indication of any vibration problems during any of the high-speed testing at FIRL using the compliant-pivot configuration.

4.3 LOAD TESTING

The load testing produced three significant milestones with respect to compliant bearing performance:

1. In one instance, the loading tape ruptured which applied a shock load to the bearings. The bearings accepted the shock load without appreciable damage.

2. Over-load contact occurred on the small (1.4 x 1.4 inch) bearing at approximately 19 psia average loading. The contact produced wiping of the heavily loaded pad.

3. After load contact occurred, the bearings were re-run without rework. The rig was run to full speed and partial load was applied without incident.

Taped information was replayed on a Fast Fourier Transform (FFT) Computing Spectrum Analyzer which produced frequency and amplitude vs. time. Figure 4-9 shows oscilloscope traces of the shaft in the dead-rest position which provides a reference for absolute shaft displacements. Each major subdivision represents 1 mil for a 200 MV scale.

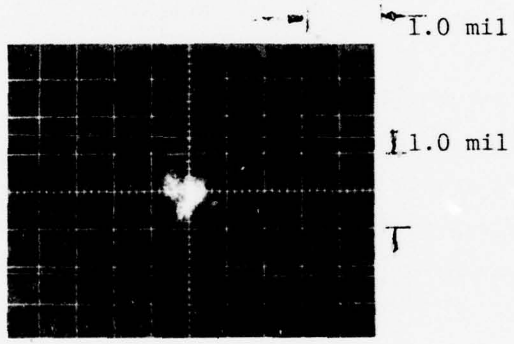

Outboard End

SHAFT SPEED - 76000 RPM

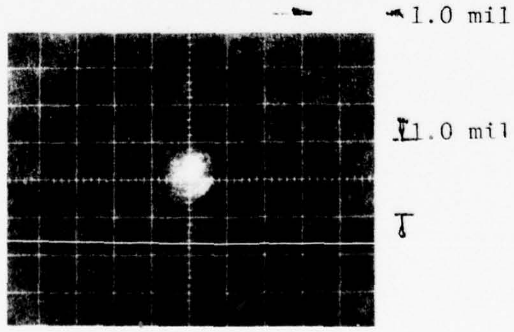

Inboard End

Figure 4-6. Shaft Orbits, High-Speed Testing

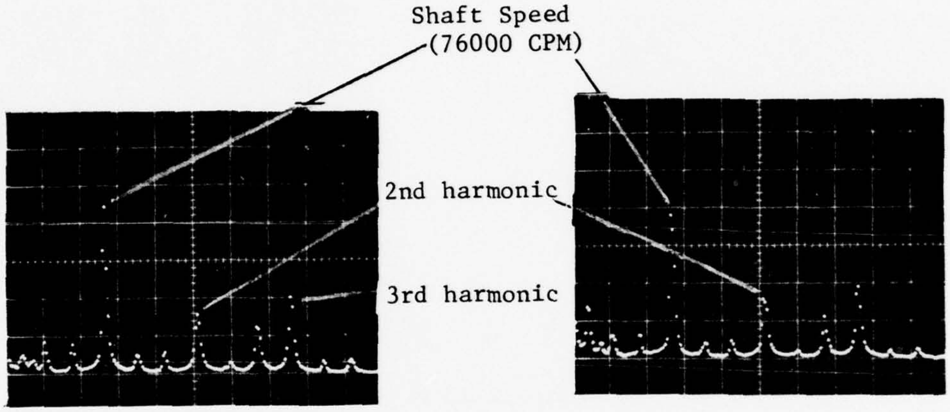

Outboard End

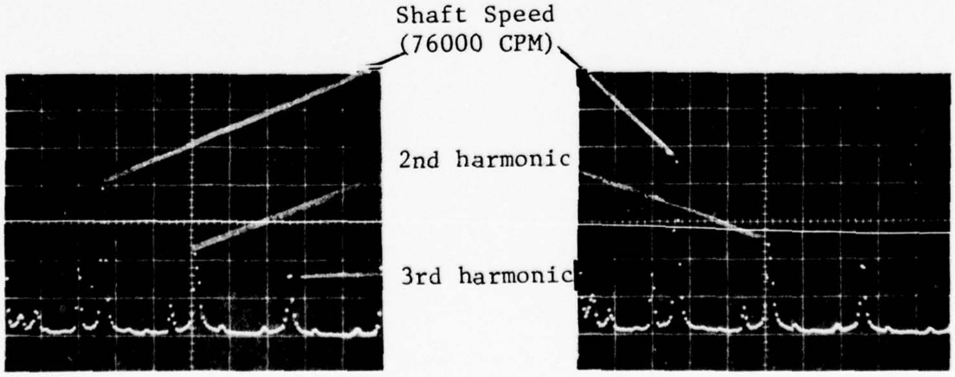

Inboard End

Figure 4-7. Frequency Spectrum, High Speed Testing

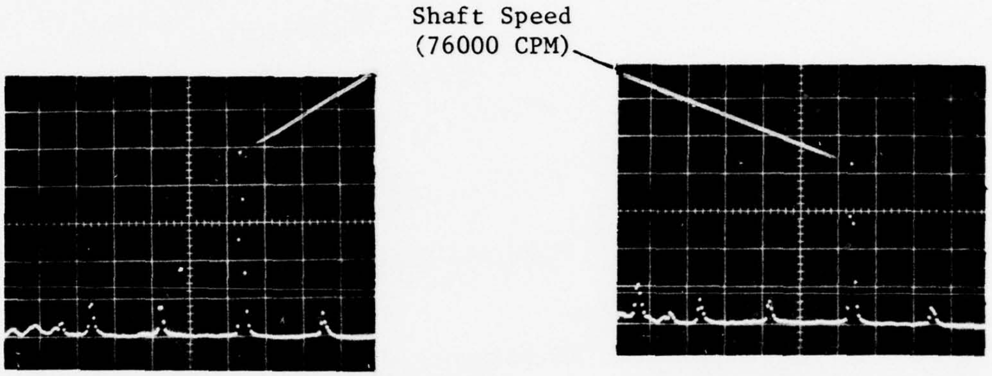

Outboard End

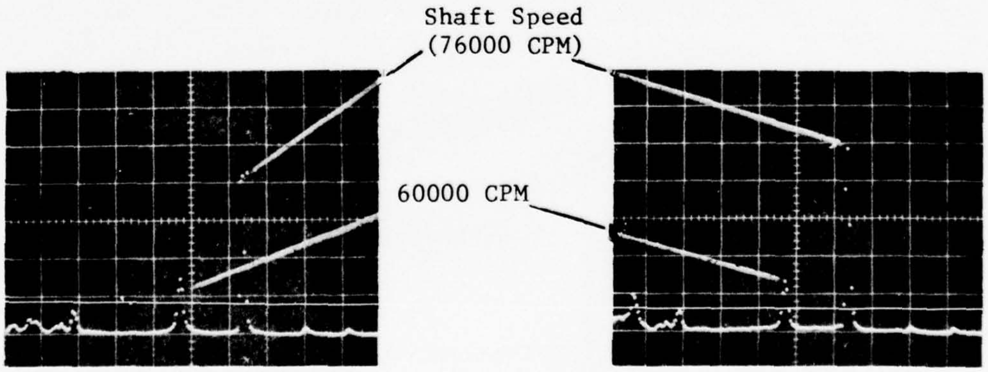

Inboard End

Figure 4-8. Frequency Spectrum, Reduced Range, High-Speed Testing

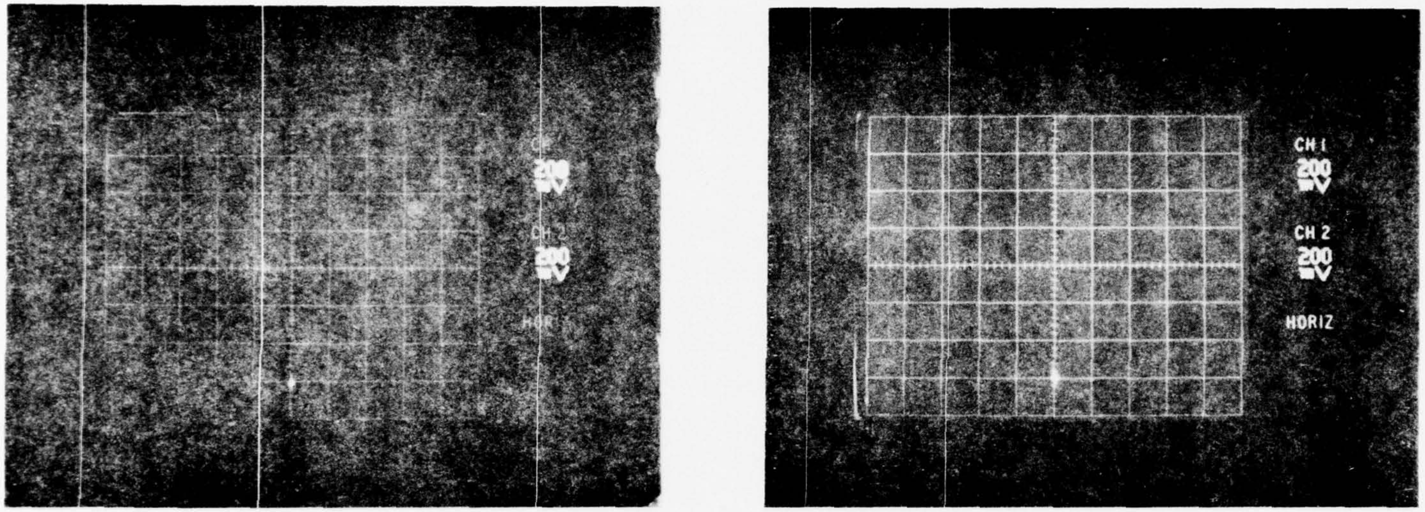

OUTBOARD

INBOARD (TURBINE)

Figure 4-9. Dead Rest Position of Shaft

I-C4965

Figure 4-10 shows operation at 58,500 rpm with loads of 27.5 lbs to the outboard (1.4 inch diameter) bearings and 29 lbs to the inboard (1.8 inch diameter) bearing. The position of the shaft is approximately 1.5 mils from the dead-rest position with a total orbit diameter of about 0.5 mils. The orbital pattern includes shaft surface imperfections. Also shown on Figure 4-10 are photographs of frequency spectrum plots produced by the FFT analyzer. On the outboard bearing the frequency is predominantly synchronous with a maximum amplitude of 0.208 mils. The inboard bearing displays a strong fourth harmonic, which is probably due to the effect of the four impulse nozzles of the air turbine (the inboard bearing is in close proximity to the turbine).

Figure 4-11 shows the orbital response and the position of the journal before and after the loading tape ruptured. The two top photographs show the outboard and inboard bearings (outboard-left, inboard-right) just prior to tape rupture (31.4 lbs on outboard bearing). Similarly, the bottom photographs indicate what occurred after the tape broke. Note that the shaft rose almost 5 mils on the outboard bearing and 2-1/2 mils on the inboard bearing. The frequency response, after tape rupture is shown on Figure 4-12. At the outboard bearing the shaft predominant frequency was synchronous, while at the inboard bearing a strong fourth harmonic was present. Figure 4-13 shows the condition of the outboard bearing after tape rupture. There was no serious damage. The most noticeable effect was a slight polishing of the spring-loaded shoe around its periphery. The bearings were reinstalled in the test rig and testing proceeded.

Overload contact occurred at loads of 37.18 lbs on the outboard bearing which produced 39.12 lbs (approximately 19 psi) on the inboard bearing. It was the outboard bearing that contacted. Figure 4-14 shows a time averaged orbital response of each bearing immediately after overload contact. Note the scale of the outboard is 2-1/2 times that of the inboard bearing, so that each major sub-division is 2-1/2 mils. The vertical excursion of the outboard bearing was over 10 mils. Figure 4-15 shows the condition of the outboard bearing after overload contact.

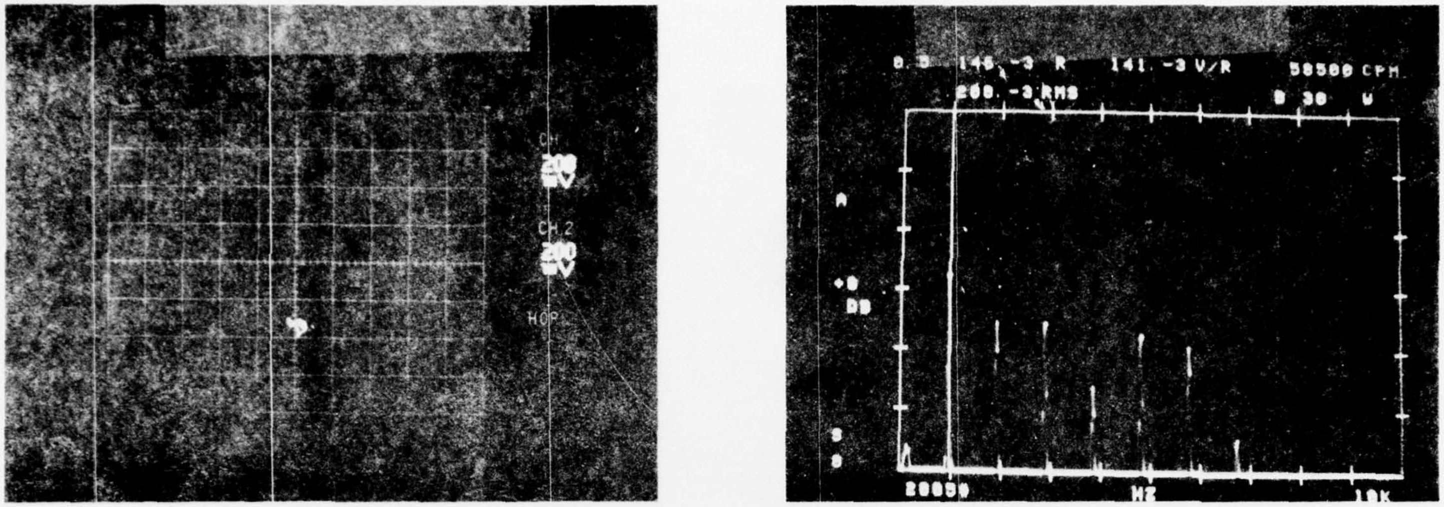

OUTBOARD BEARING
W = 27.5 LBS
N = 58,500 CPM

OUTBOARD BEARING

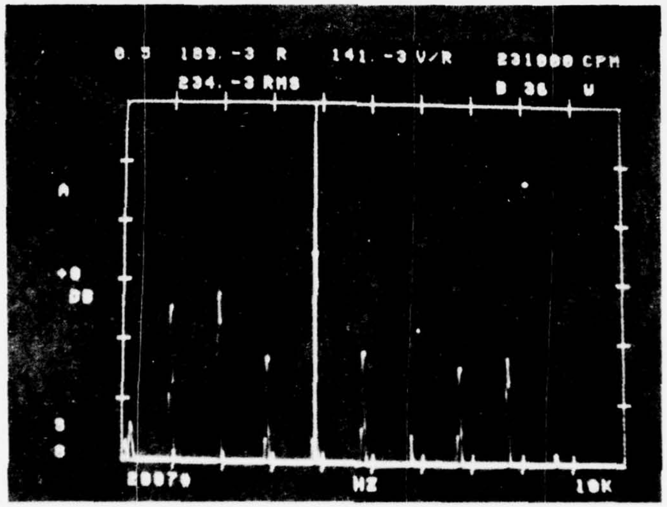

INBOARD BEARING
W = 29 LBS
N = 58,500 CPM

Figure 4-10. Oscilloscope and Spectrum Traces

I-C4965

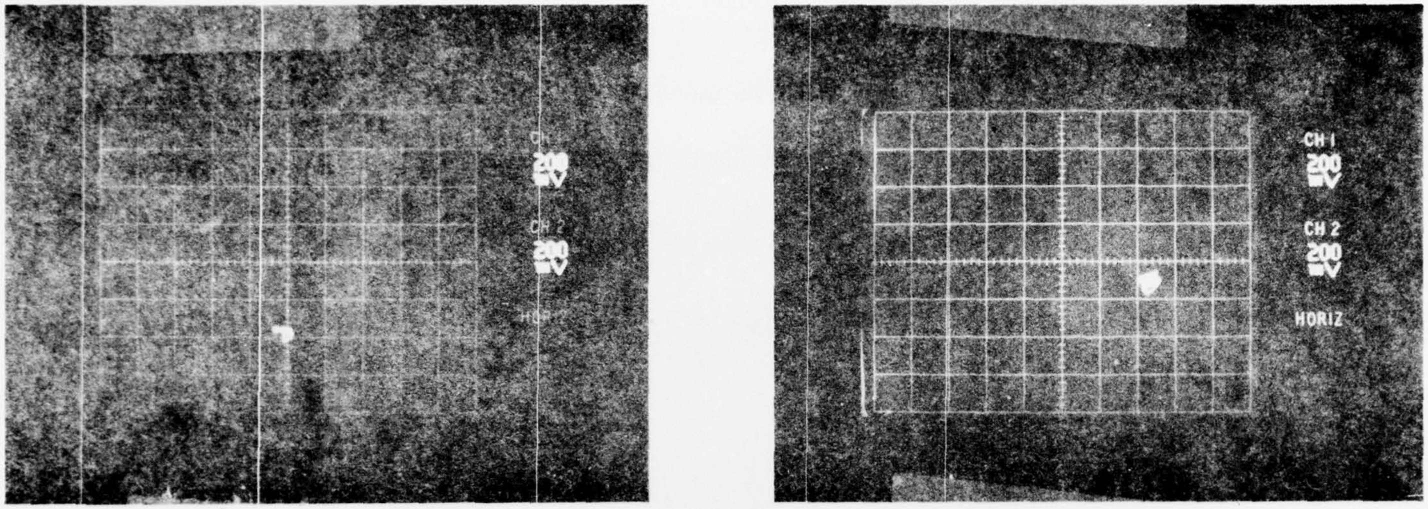

W = 31.37 LBS

W = 33.1 LBS

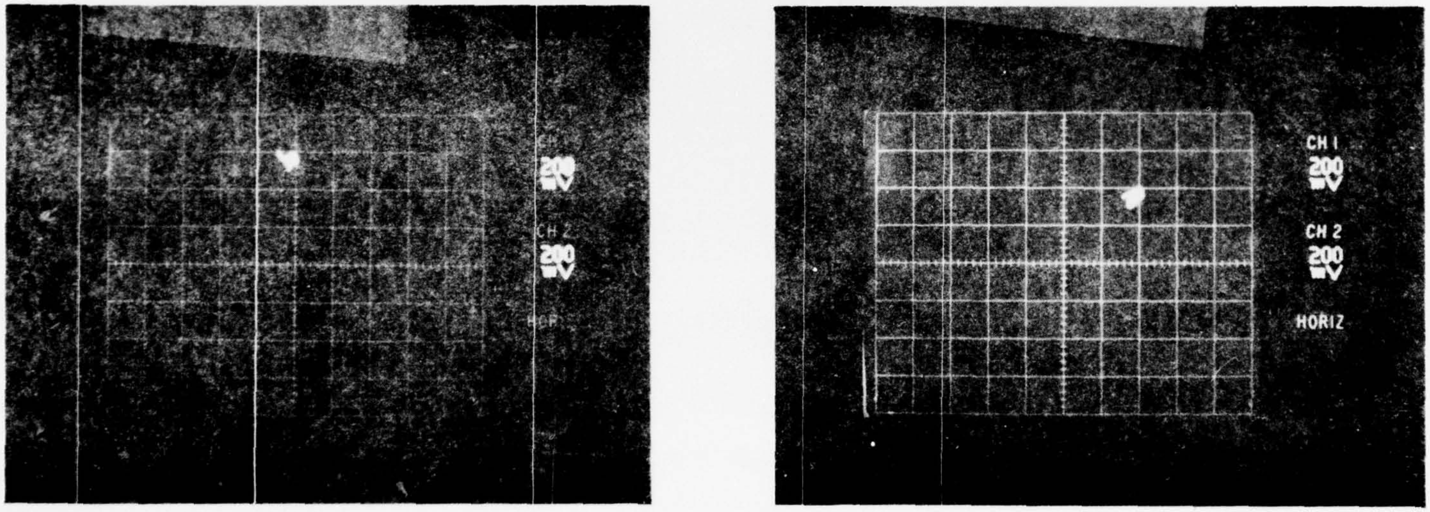

W = 5.4 LBS

W = 8.4 LBS

I-C4965

Figure 4-11. Outboard-Inboard Orbital Positions Before and After Tape Broke

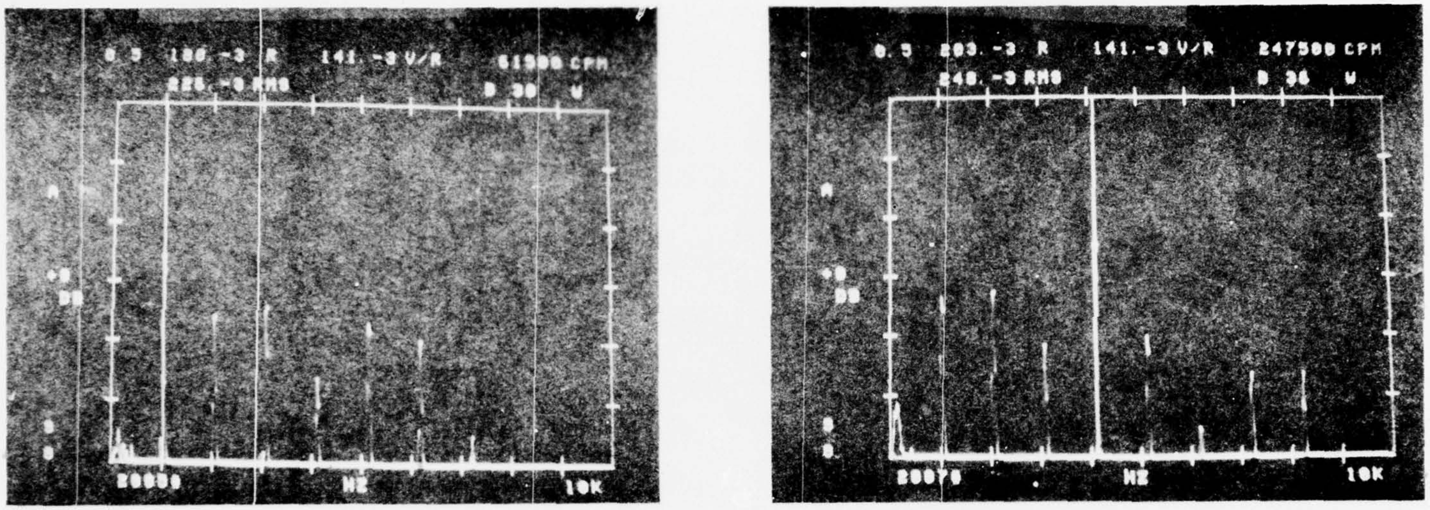

OUTBOARD HORIZONTAL
W = 5.48 LBS

INBOARD HORIZONTAL
W = 8.4 LBS

Figure 4-12. Frequency Spectrums After Tape Ruptured

I-C4965

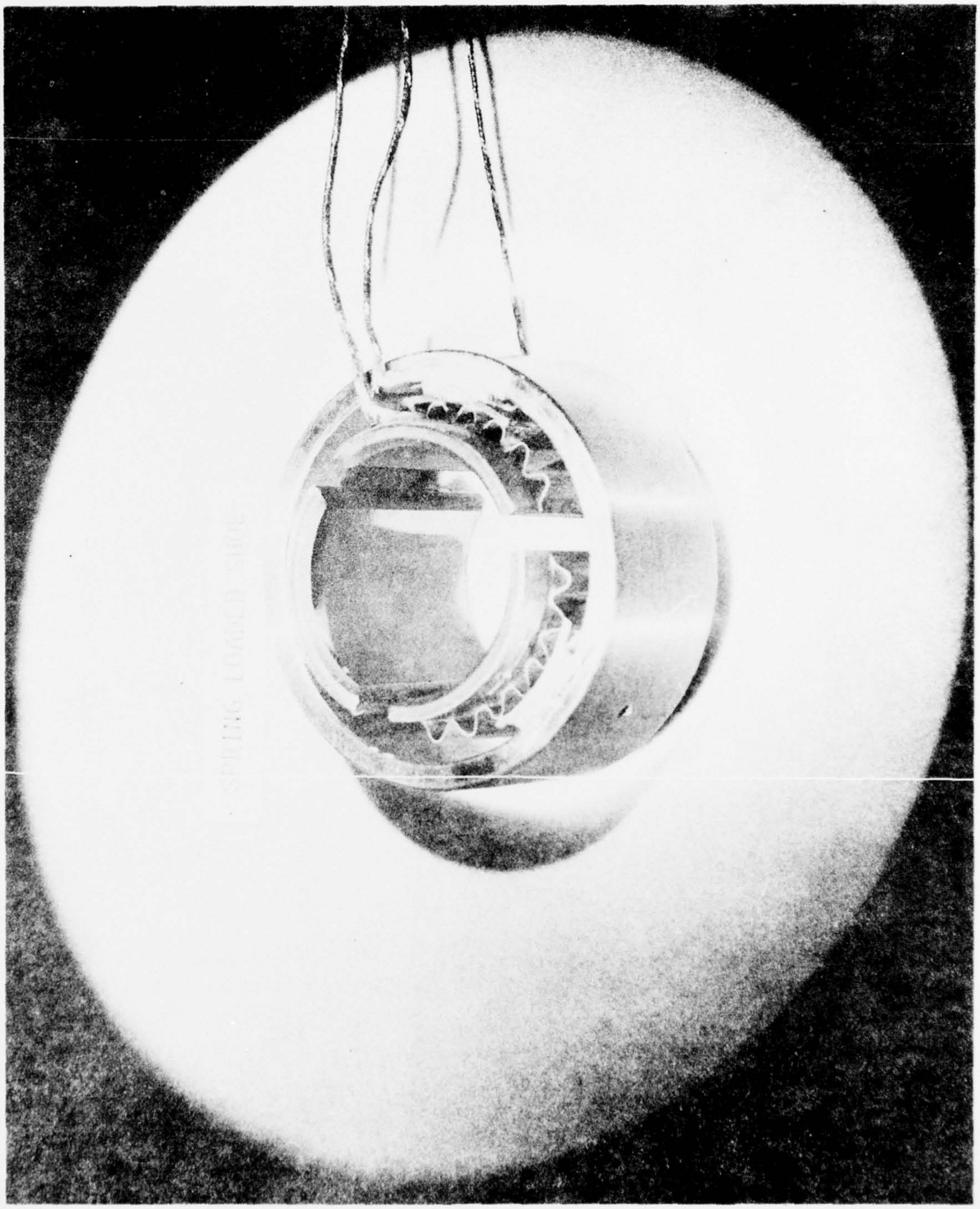

Figure 4-13. Condition of Outboard Bearing After Tape Rupture

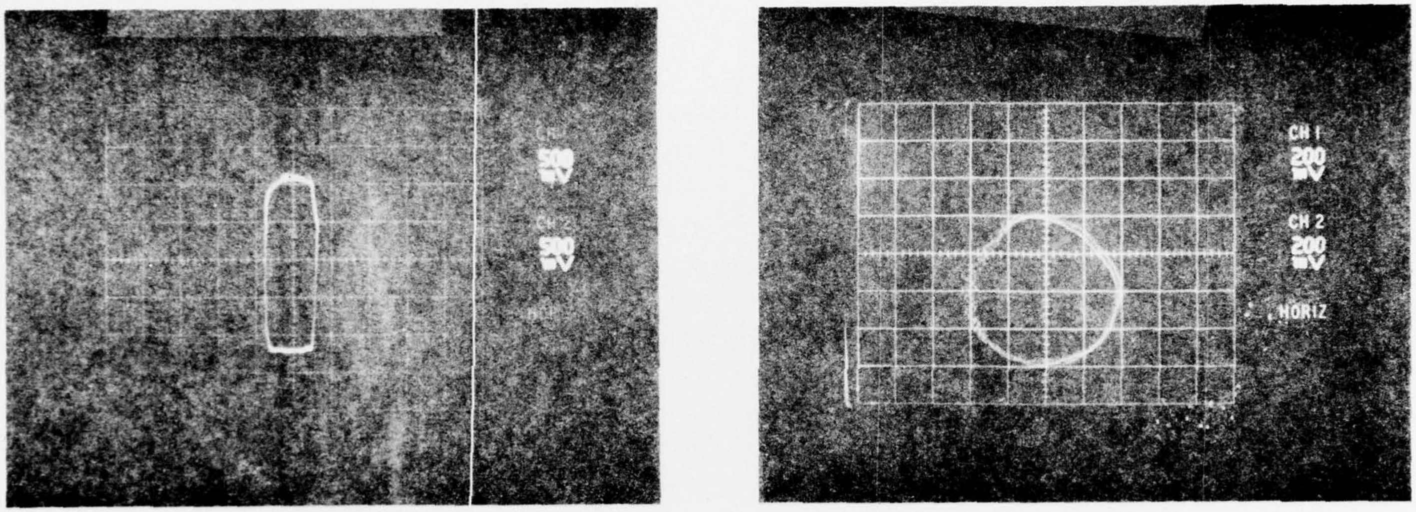

OUTBOARD
W = 37.18 LBS
(18.97 PSI)

N = 60,000 RPM

INBOARD
W = 39.12 LBS
(12.07 PSI)

Figure 4-14. Bearing Excursion Immediately After Outboard Bearing Contact

I-C4965

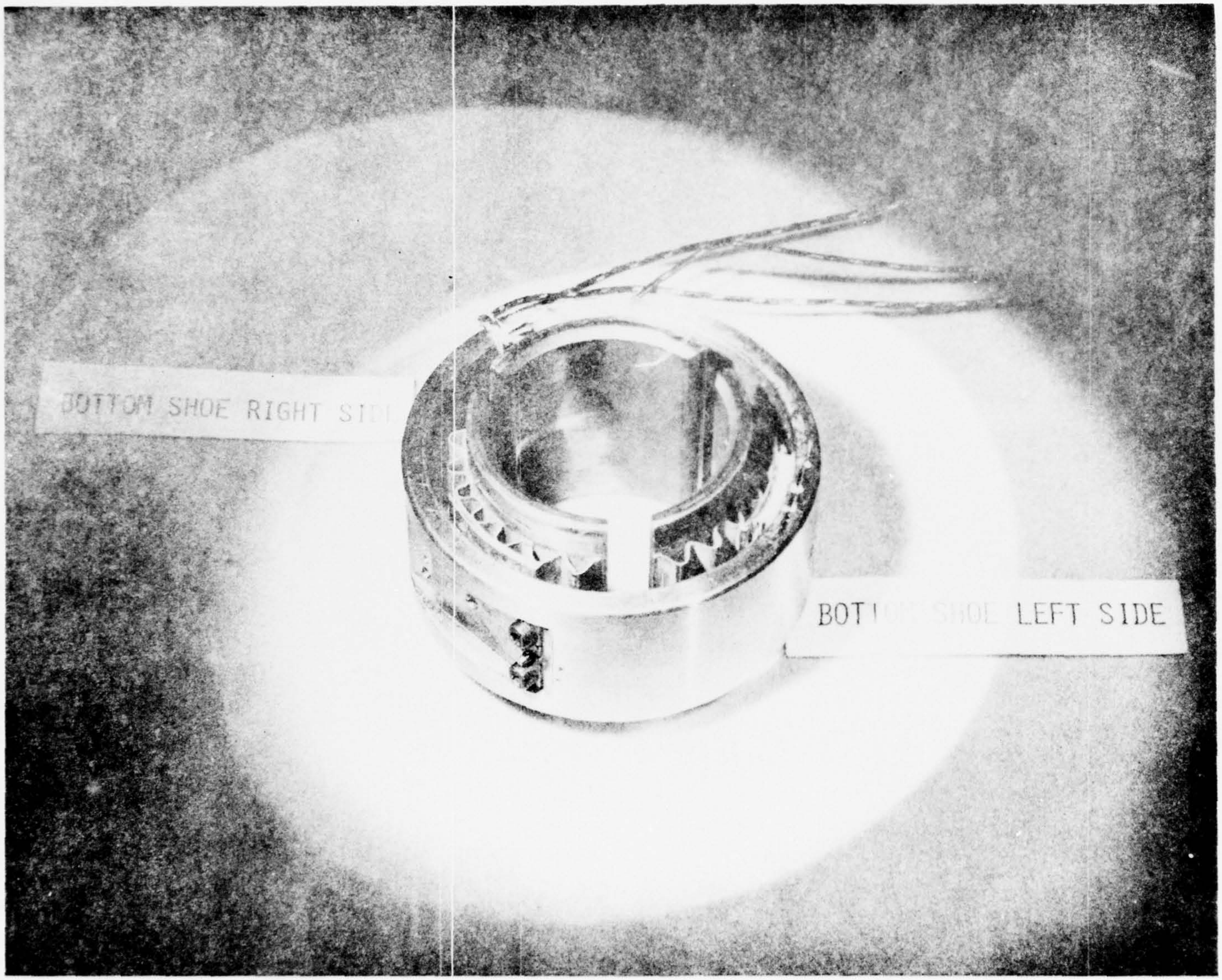

I-C4965

Figure 4-15. Condition of Outboard Bearing After Overload Contact

A definite surface wipe is evident, although degradation of the surface was not obvious to the touch.

Figure 4-16 shows the condition of the shaft after overload contact. There was obvious transfer of graphite material to the shaft at the small diameter end. Without further rework the bearings were reinstalled in the rig, and it was run to 70,000 rpm with 27.5 lbs applied to the outboard bearing (14 psi) without any noticeable degradation of performance.

Theoretical computations were previously discussed and results are repeated on Figure 4-17.

On the basis of the theoretical results, contact occurred at 37 lbs with an operating pivot film thickness of 0.18 mils. It is concluded that for all practical purposes 19 psi represents the maximum load capacity of compliant-mounted bearings.

4.4 OPERATING TEMPERATURES OF BEARINGS

Bearing temperatures were recorded before and after contact. Temperature values before contact occurred are as follows:

Location	Temperature
Inboard Bearing Inboard End	184°F
Inboard Bearing, Outboard End	179°F
Outboard Bearing, Inboard End	186°F
Outboard Bearing Outboard End	155°F

These temperatures are representative of high-load conditions. They are not excessively high and did not pose a danger to the elastomer.

I-C4965

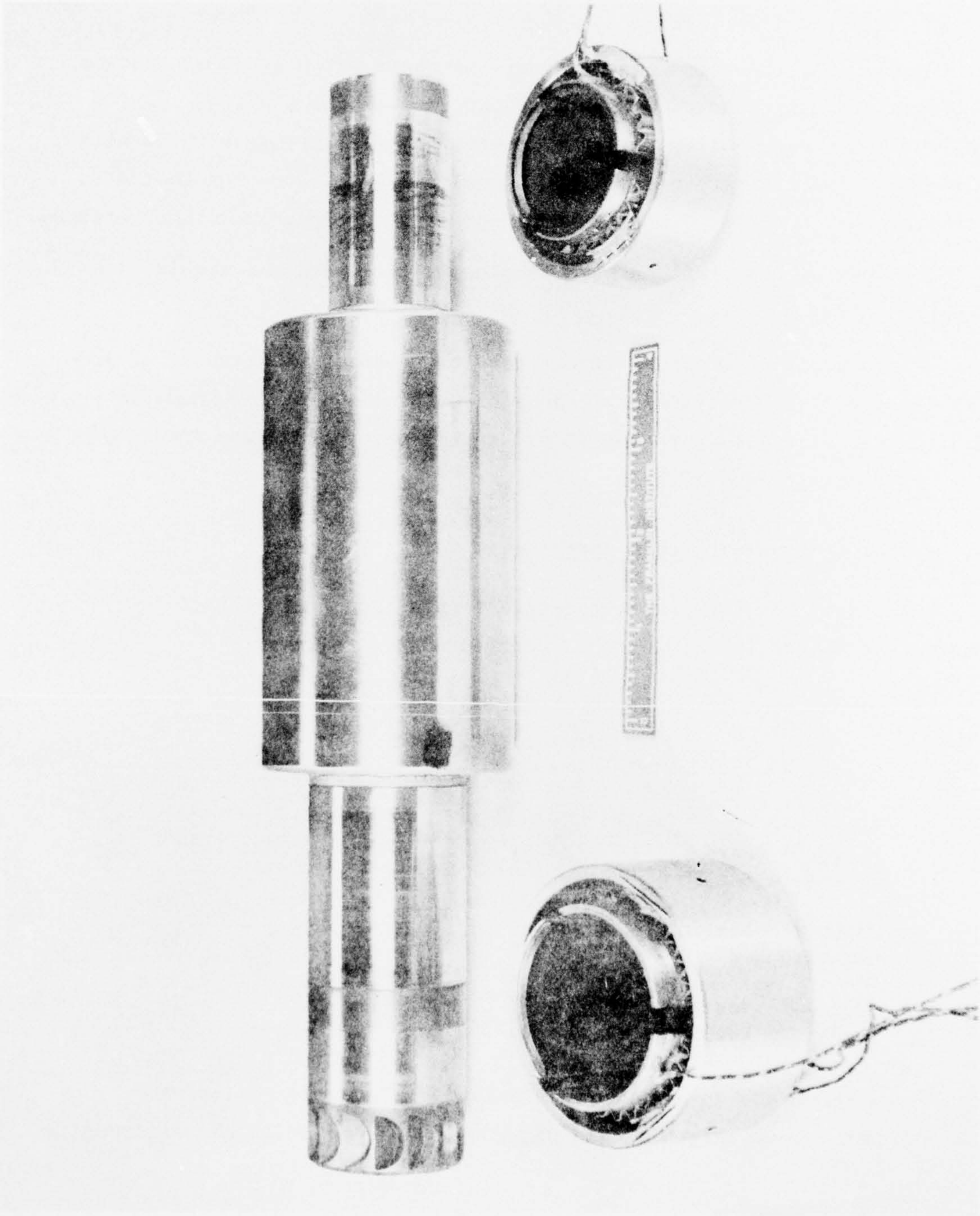

Figure 4-16. Condition of Shaft After Overload Contact

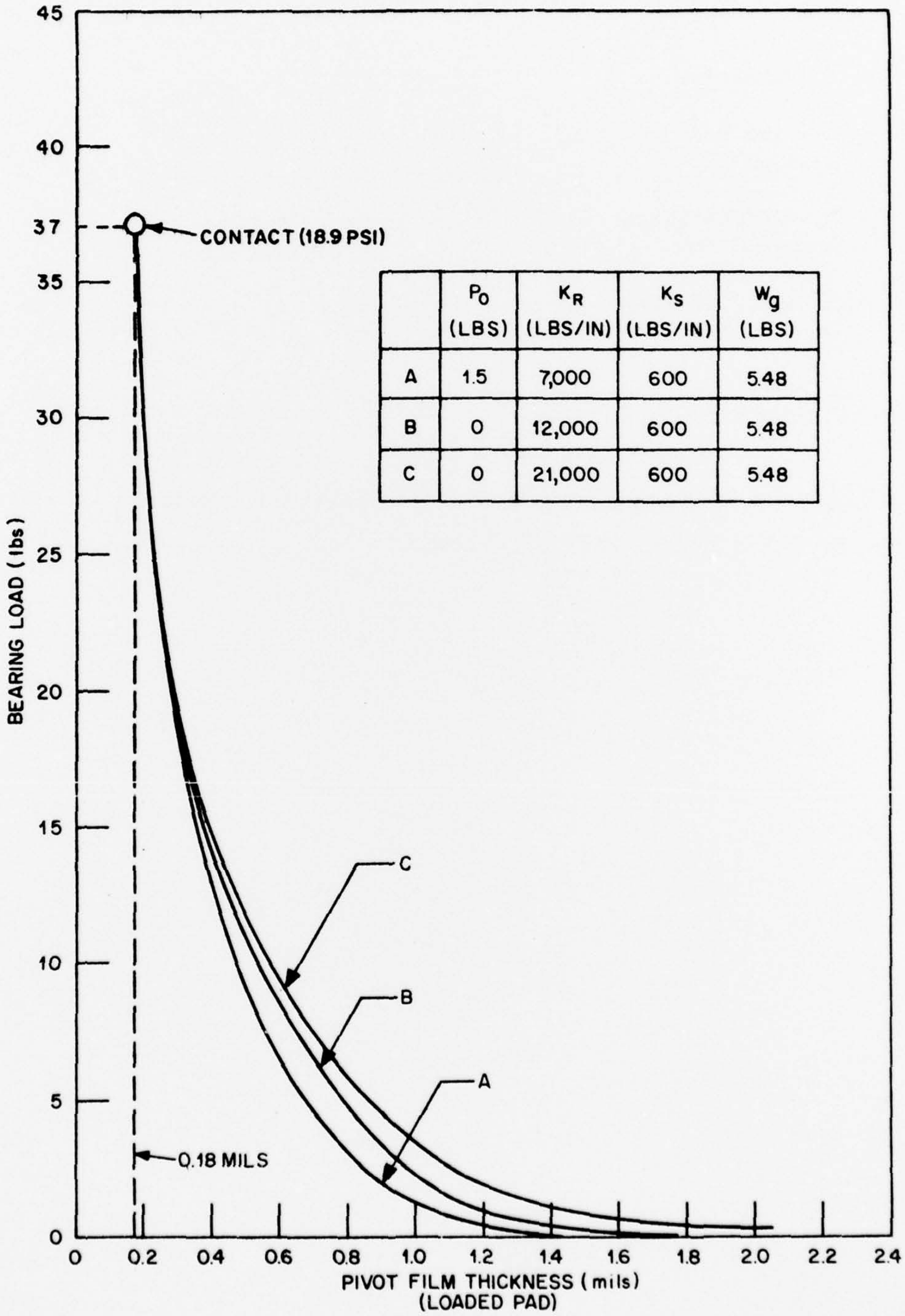

	P_0 (LBS)	K_R (LBS/IN)	K_S (LBS/IN)	W_g (LBS)
A	1.5	7,000	600	5.48
B	0	12,000	600	5.48
C	0	21,000	600	5.48

Figure 4-17

Following the contact, the maximum temperatures recorded were as follows:

Location	Temperature
Inboard Bearing, Inboard End	182°F
Inboard Bearing, Outboard End	174°F
Outboard Bearing, Inboard End	430°F
Outboard Bearing, Outboard End	500°F

Although temperatures reached 500°F, subsequent operation of the bearings was not significantly affected.

5. CONCLUSIONS AND RECOMMENDATIONS

As a result of the program described in this report the following are the significant conclusions:

- The compliant-pivot journal bearing demonstrated whirl-free capability at high speed (76,000 rpm).
- The bearing was capable of accepting high loading, 19 psi, which is probably representative of maximum loading capability on an air lubricated, compliant-pivot journal bearing.
- The bearing demonstrated capability of accepting shock loading without becoming inoperative.
- The bearing withstood high-load, high-speed rub and was subsequently operative without rework.
- Further information concerning small displacement stiffness properties of elastomers would be helpful to the theoretical analyses of compliant-pivot bearings. It is probably necessary to account for the non-linear stiffness effects of the elastomer mounting.

6. ACKNOWLEDGEMENT

In addition to the support of ONR in the development of compliant-pivot bearings, acknowledgement is made to a parallel program supported by the U.S. Army Mobility Equipment Research and Development Center at Fort Belvoir, Virginia reported upon by reference [1].

7. REFERENCES

1. W. Shapiro and R. Colsher, "Development of Compliant-Mounted Gas Bearings for a Small, High-Speed, 10 KW Turboalternator," Franklin Institute Research Laboratories report dated September 1976 for U.S. Army Mobility Equipment Research and Development Command, Fort Belvoir, Virginia, Contract DAAK02-72-6-0571.

2. W. Shapiro, R. Colsher and F. Kramberger, "Development of Compliant-Mounted Gas Bearings for a High-Speed Turbomachine," SAE Paper 751071, published in SAE Transactions, 1975, pp. 2989-3003.

3. W. Shapiro, "Compliant Mounted Bearings and Their Application," ASME paper 77-DE-18.

4. A. N. Gent and E. A. Meinecke, "Compression, Bending and Shear of Bonded Rubber Blocks," Polymer Engineering and Science, January 1970, Volume 10, No. 1

5. W. Shapiro and R. Colsher, "Analysis and Design of Gas-Lubricated, Tilting-Pad Journal Bearings for Miniature Cryogenic Turbomachinery," Technical Report AFFDL-TR-70-99, August 1970, for Air Force Flight Dynamics Laboratory, U.S. Air Force Systems Command, Wright-Patterson Air Force Base, Ohio.